Ultraconfined 1-nm water as nature-inspired electrolyte for blue batteries

Vasily Artemov[1*], Svetlana Babiy[2], Yunfei Teng[1,3], Jiaming Ma[4], Alexander Ryzhov[5], Tzu-Heng Chen[1], Lucie Navratilova[6], Victor Boureau[6], Pascal Schouwink[7], Mariia Liseanskaia[8], Patrick Huber[8,9], Fikile Brushett[10], Lyesse Laloui[2], Giulia Tagliabue[4], Aleksandra Radenovic[1,3*]

[1]Laboratory of Nanoscale Biology (LBEN), École Polytechnique Fédérale de Lausanne (EPFL), Lausanne, 1015, Switzerland.
[2]Soil Mechanics Laboratory (LMS), École Polytechnique Fédérale de Lausanne (EPFL), Lausanne, 1015, Switzerland.
[3]NCCR Bio-Inspired Materials, École Polytechnique Fédérale de Lausanne (EPFL), Lausanne, 1015, Switzerland.
[4]Laboratory of Nanoscience for Energy Technologies (LNET), École Polytechnique Fédérale de Lausanne (EPFL), Lausanne, 1015, Switzerland.
[5]Center for Transport Technologies, Austrian Institute of Technology (AIT), Vienna, 1210, Austria.
[6]Interdisciplinary Center for electron microscopy (CIME), École Polytechnique Fédérale de Lausanne (EPFL), Lausanne, 1015, Switzerland.
[7]X-ray Diffraction and Surface Analytics Platform (XRDSAP), École Polytechnique Fédérale de Lausanne (EPFL), Lausanne, 1015, Switzerland.
[8]Institute for Materials and X-ray Physics, Hamburg University of Technology (TUHH), Hamburg, 21073, Germany.
[9]Deutsches Elektronen-Synchrotron DESY, Hamburg, 22607, Germany.
[10]Department of Chemical Engineering, Massachusetts Institute of Technology (MIT), Cambridge, 02139, MA.

*Corresponding author(s). E-mail(s): vasily.artemov@epfl.ch; aleksandra.radenovic@epfl.ch;

Abstract

Artificial engineering often relies on scarce materials, possessing ecological, social, and political risks. In contrast, nature achieves advanced functionalities using only abundant elements and water. Despite this simple insight, incorporating nature-inspired devices made from readily available resources into industrial applications remains a formidable challenge. Here, we present a sustainable 'blue battery'—a water-based energy storage device that mimics natural processes and reduces dependence on scarce materials. This battery harnesses the distinctive electrical properties of water confined within nanometer-scale pores, enabling construction from abundant, non-toxic materials using scalable nanofabrication techniques. It operates without unwanted side reactions, maintains nearly 100% efficiency after 60,000 charge-discharge cycles, and supports a voltage window of up to 1.65 V while achieving competitive power and energy density. The core component, a van der Waals clay nanostructure, uses water as the sole electrolyte with enhanced activity due to interactions with its 2D surface. This water-driven technology offers a sustainable platform for energy systems, with potential applications from small-scale electronics to global energy infrastructure—even in extreme environments like Mars. Our work advances nature-inspired energy solutions, opening new possibilities for the sustainable engineering of blue devices.

1 Main

In contrast to man-made engineering approaches, nature builds its functionalities using abundant 'primitive' chemical elements and water, prioritizing nanoscale structuring over the optimization of chemical composition [1–3]. This strategy, which ensures scalability and growth critical for survival [4], presents a blueprint for engineering innovations aimed at sustainability. By mimicking nature, we can reduce dependence on scarce materials and develop water-based systems—hereafter referred to as 'blue devices'—which hold the potential to meet rising demands in areas such as sustainable batteries [5], neurointerfaces [6], and neuromorphic computing [7]. However, a thorough understanding of water's atomic and molecular behavior at interfaces, a topic of growing interest in recent years [8–13], remains essential for advancing these technologies.

Recent studies have revealed unusual properties of water confined in pores ranging from a few angstroms to several nanometers, or ultraconfinement [14–16]. Under these extreme conditions, water exhibits behavior distinct from bulk water, challenging existing theoretical models [17]. Experiments have revealed unique effects such as dielectric polarization anisotropy and protonic 'superconductivity,' both linked to altered proton dynamics in ultraconfined water [18–21]. These discoveries open exciting possibilities for blue devices, particularly in improving aqueous batteries and supercapacitors. These devices offer safer, more cost-effective alternatives to traditional technologies that rely on metal oxides and concentrated electrolytes [22, 23], and are crucial for stabilizing renewable energy networks powered by solar and wind. While previous efforts in nanofluidic systems have demonstrated impressive performance in energy applications [24, 25], scaling them up for practical use remains a significant challenge [26, 27].

Utilizing ultraconfined water in nature-inspired designs with abundant materials could unlock new scaling-up possibilities while addressing environmental and sustainability concerns.

In this work, inspired by nature, we introduce a sustainable 'blue battery.' This water-based device utilizes pure water confined within extremely narrow 1-nm-high slit pores as an electrolyte, where proton activity is significantly enhanced compared to bulk water. We demonstrate that few-molecule-high water channels facilitate the separation and accumulation of protons and hydroxides within the electrodes' electrical double layers (EDLs). To ensure practical applicability, the device is constructed exclusively from abundant materials—clay, graphene, and water—reducing reliance on scarce resources in energy storage. The device achieves up to 100% coulombic efficiency, with a projected equivalent lifespan of 150 years without significant degradation. It operates within a voltage window of 1.65 V, offering competitive power and energy densities. By focusing on precise structural design rather than rare chemical elements, our 'blue battery' provides a scalable and sustainable platform for various future technologies. These include safe energy storage systems, electrolyzers, bio-computer interfaces, and neuromorphic devices, where ultraconfined water within solids serves as both an electrolyte and a separator.

1.1 Topologically connected channels as blue device concept

Unlike previous aqueous electrochemical systems with geometrically disjointed electrodes (Fig. 1, a and b), we introduce a topologically connected membrane-electrode unit (Fig. 1c), which mimics natural systems such as the interstitial fluid in biological organisms (Fig. 1d), providing structural continuity within tissue and organ boundaries [28]. Consider the simplest aqueous capacitor, the 'Leyden jar' [29], which consists of two metal electrodes in contact with water (Fig. 1a). In this device, electric energy is stored in a thin, nanometer-scale interface (blue glow) with a low energy density due to a negligible surface-to-volume ratio. To improve this, the classic battery or supercapacitor design (Fig. 1b) increases the surface area of the electrodes to enhance energy density but also increases an electrolyte concentration to secure high current density, thereby promoting chemical complexity. In contrast, we propose transforming the disjointed electrodes into a unified, topologically connected network of electrical double layers (EDLs) without involving bulk water (Fig. 1c). This design leverages the unique properties of ultraconfined water without increasing chemical complexity, maintaining sustainability without compromising performance.

To design our blue device, we created an electrode-membrane-electrode unit out of abundant 2D materials loaded with ultraconfined water within 1-nm-high slit channels (Fig. 1e). In the channels the walls are so close that the double layers of water from opposite sides overlap, eliminating bulk water and leaving only interfacial water with affected self-dissociation-recombination balance [17]. Such water exhibits modified electrodynamic properties and an increased activity of H^+ and OH^- ions. Additionally, the EDLs of the electrodes connect topologically through the EDLs of the separator, creating a continuous network across the device parts. This design mimics nature by focusing on space structuring rather than chemical diversity. As demonstrated below, the device achieves exceptional cycle life and competitive performance. Water access

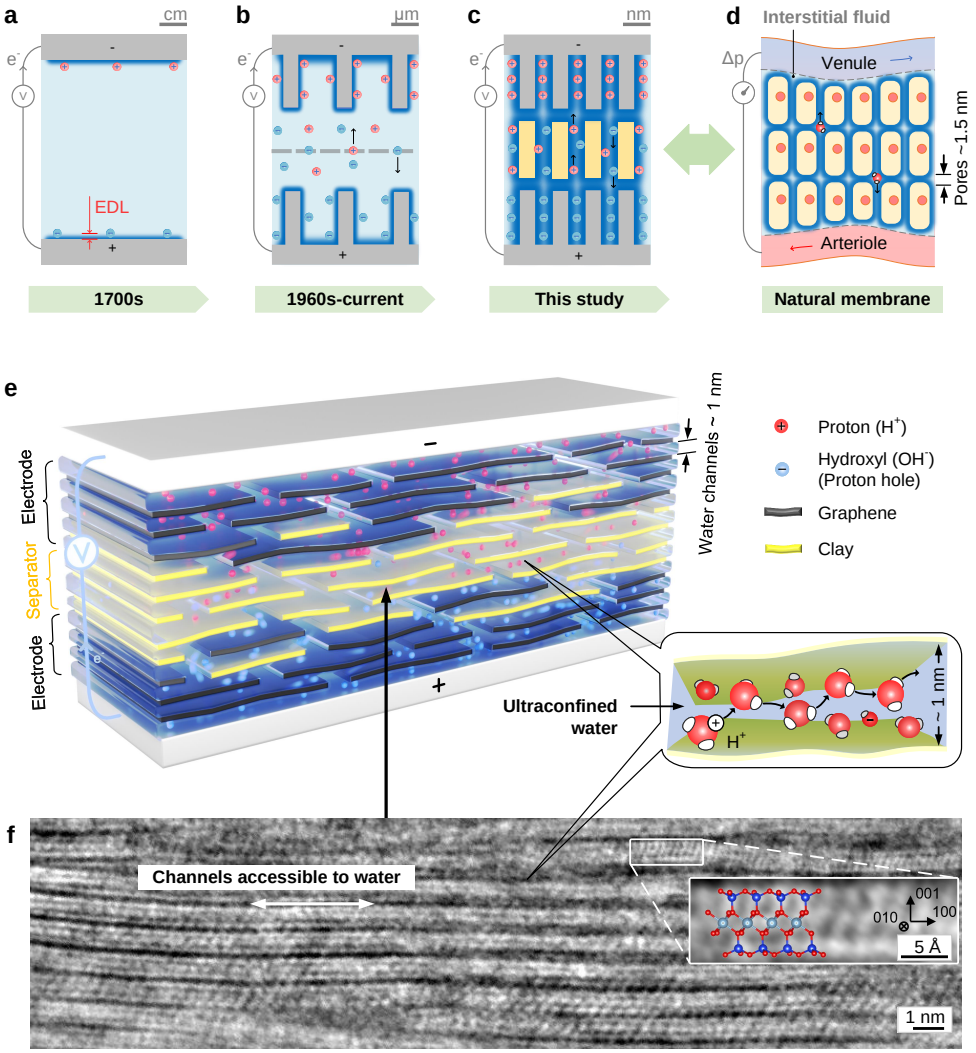

Fig. 1 Blue device concept. Evolution of charge separation systems: (**a**) a first water 'battery'—the Leyden jar—with two metals in water; (**b**) modern battery, supercapacitor, or electrolyzer with two high-surface-area electrodes in an electrolyte; (**c**) topologically non-equivalent to (a) and (b) 'blue battery' of this study with continuously intercalated by ultraconfined water nano-dimensional space of electrodes and separator. (**d**) Nature analogy: the section of body tissue with continuous fluid space between living cells (interstitium) extending throughout the entire organism, connected to the lymph, and functioning like an electrolyte. Blue glow depicts an electrical double layer (EDL) with enhanced electrolytic properties. (**e**) Schematic illustration of the blue device (supercapacitor) designed in this study, consisting of a vdW structure of graphene and clay with water in 1-nm channels serving as a sole electrolyte. (**f**) Cross-sectional image of the smectite-clay separator from the real device by integrated differential phase contrast (iDPC) scanning transmission electron microscopy (STEM), showing channels accessible to water. The inset shows an atomic-resolution close-up with the corresponding crystal structure overlapped. Red, blue, and cyan dots are for O, Si, and Al atoms, respectively.

into the aligned slit pores (Fig. 1f) is ensured by the use of hydrophilic clay, whose properties require a separate analysis at the microscopic level.

1.2 Where water meets Earth: clays as natural 2D materials

Clays occur on all Earth's continents (Fig. 2a) and also on Mars [30]. On the microscopic level, they have fine crystalline structure (Fig. 2b) [31]. The most common types of clay—kaolinite, illite, and smectite (Fig. 2c)—consist of 1-nm-thick crystals made of silica and alumina planes, interchanging differently depending on the clay type to form flat flakes. These flakes are held together by vdW interactions, forming periodic heterostructures up to micrometers in size (SI Figs. S1-S4). Natural clays are chemically simple and composed of silicon, oxygen, and aluminum atoms but may also include water-soluble potassium, sodium, or calcium, which can be reversibly substituted by, e.g. hydrogen [31, 32].

Unlike synthetic vdW heterostructures [34, 35], clays offer several advantages: low price, scalability, widespread availability, natural affinity to water, safety, and biocompatibility. Their organized slit channels (Fig. 2b) facilitate water and proton transport [32], allowing for the movement and relative separation of positive and negative ions under natural conditions or an external electric field. Besides intercellular spaces (Fig. 1d), the clay interlayer pores are similar to small wood pores or nerve cell structures [36, 37], making them suitable for nature-mimicking engineering.

Our X-ray diffraction (XRD) analysis showed that exposing dried clays to saturated water vapor or liquid water results in interlayer expansion or swelling, evidenced by diffraction peak shifts (Fig. 2e and SI Figs. S5 and S6). This process and the natural clay structure allow the creation of periodic slit channels filled with water (Fig. 2d). Notably, this procedure is much less expensive and time-consuming than the artificial vdW channels design [38] and has almost infinite materials sourcing capabilities. We found that smectite, in particular, has an equilibrium pore height of ~ 1 nm, consistent with previous reports [39, 40]. Coincidentally, these dimensions correspond to the peak maximum of proton conductivity observed in water confined in a nanoporous medium and within artificial slit pores [18, 20, 21].

To test the electrical properties of clays, we first carefully cleaned the samples and then hydrated them in saturated water vapor (see Methods for sample preparation). This process ensured the absence of contamination and foreign ionic impurities. Dry clays acted as good insulators, while wet clays conducted ions with the assistance of water. We observed significant ionic conductivity in all wet clays, in contrast to both bulk water and dry clays, which exhibited high resistivity ($\sim$1 MΩ·cm, Fig. 2f). Smectite, in particular, demonstrated the highest direct-current (DC) conductivity of 0.6 S/m, comparable to that found in synthetic slits and ceramics [20, 21], and equivalent to the conductivity of a 0.1-M NaCl solution in bulk water or ionic liquids [41]. Notably, this conductivity is six orders of magnitude greater than that of bulk water, which is $0.6{\cdot}10^{-7}$ S/m [17] (see blue dashed line).

The enhanced ionic transport in hydrated clay can be understood via dynamic interactions between the water and the clay under conditions of ultraconfinement. The natural substitution of Si^{4+} and Al^{3+} atoms in the clay's crystal structure by Al^{3+} and Mg^{2+}, respectively, creates an excess negative surface charge [31]. In nature, this excess

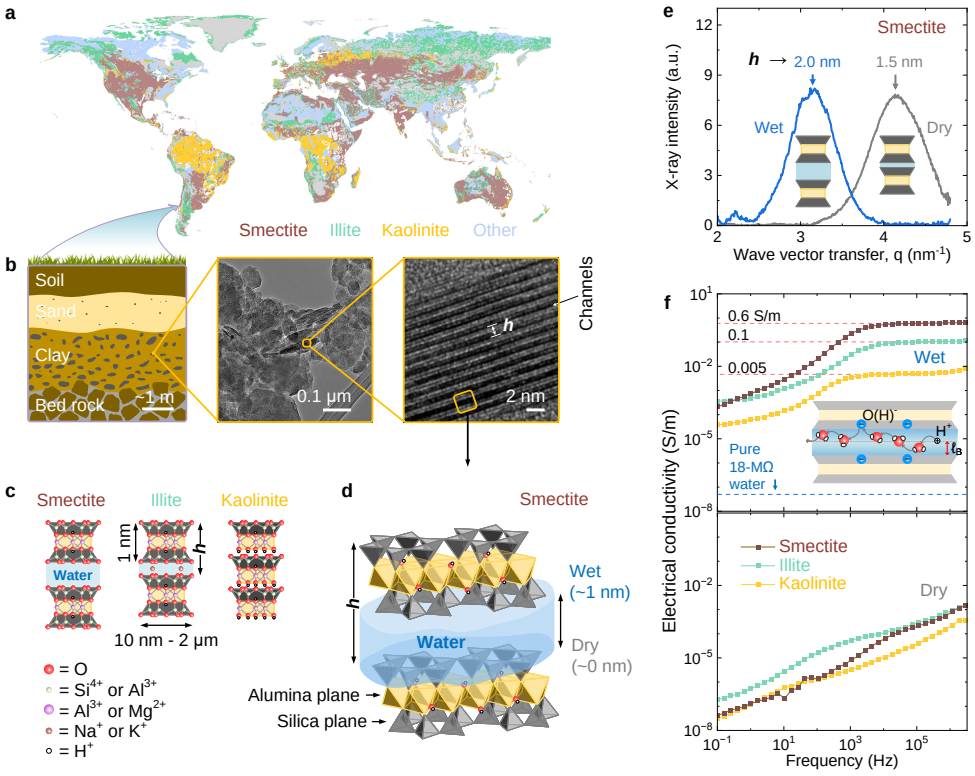

Fig. 2 Clays: worldwide abundant natural 2D materials. (**a**) Clays topsoil distribution on Earth (data [33]). Colors show regions with the areal density of clay exceeding 10 kg/m^2. (**b**) Clays at different magnifications: Meter-scale schematic soil cross-section (left), micro-scale TEM image of a clay powder (middle), and nano-scale TEM image of pristine clay crystal (right). (**c**) Three most common clay structures: smectite, illite, and kaolinite. The gray and yellow colors are for silica and alumina crystal planes, respectively; blue is for water. (**d**) Crystal structure of smectite clay. (**e**) Synchrotron small-angle X-ray scattering (SAXS) on wet and dry smectite clay powders. Peak shift indicates the change of interlayer distance h with water content. The baseline is subtracted (raw data in SI Fig. S5). (**f**) Proton conductivity of clays under wet (top) and normal (bottom) conditions. More data in SI Figs. S18-20.

surface charge is balanced by adsorbed alkaline cations to maintain electro-neutrality [31]. In cleaned clays, this role is played by H^+ (excess protons) of water, whose adsorption and desorption increase the conductivity of confined water by disrupting its self-dissociation equilibrium [42] and raising the concentration and mobility of H_3O^+ and OH^- (see inset in Fig. 2f). This effect is most pronounced in pores around 1.5 nm (approximately 2 times the Bjerrum length, $l_B = q^2/(4\pi\epsilon_0\epsilon k_B T) \approx 0.7$ nm), aligning with experimental data [20, 21] and predictions from the ionic model of water [17]. Notably, excess protons move via a relay-race proton-hopping mechanism, with water molecules acting as mediators, resulting in significantly higher mobility compared to other ions [17].

This scenario is supported by the negative surface charge we detected on colloidal nanoparticles of clays in distilled water (SI Table S1). The interaction between clay and water enables ultrahigh ion conduction within the ∼1-nm slit channels, transforming confined water into a partially ionic liquid with H^+ and OH^- ions as charge carriers. This effect, observed in other nanoconfinement systems [18, 20, 21], provides opportunities for nature-inspired engineering of blue devices. The use of clay, which processing does not require any extra chemicals unlike other 2D materials, ensures low cost and natural hydration of the system.

1.3 Energy storage in confined water: blue battery

To utilize the unique properties of ultraconfined water, including its inherent safety, giant in-plane polarizability [21], and enhanced conductance from surface-water interactions [20], we designed an electricity storage unit (blue battery). Using the nanopore vacuum filtration technique (Fig. 3a; see Methods), we sequentially and controllably self-assembled layer by layer the mixed graphene-clay vdW heterostructures to form two composite electrodes divided by a pure clay separator. The result was a scalable, free-standing membrane-electrode unit (MEU) in the form of nanocomposite film approximately 200 μm thick (Fig. 3b, c), featuring a three-layer structure (Fig. 3d), and having high stability and flexibility, typical for vdW heterostructures [38].

SEM EDX mapping (Fig. 3e, f) confirmed the presence of only clay (O, Al, Si) and graphene (C) elements (see SI Figs. S9, S10 for additional data). Electron microscopy showed that within the layers (Fig. 3g, h), material flakes are aligned to form parallel channels, which intersect at the edges of the domains (Fig. 3i). Moreover, no voids are detected at the interface between the domains of the separator and the electrodes. The channels were filled with water via capillary condensation from saturated water vapor, with mass gain used to control the process. This design promotes ultraconfined water intercalation into the electrodes and the separator while eliminating bulk-water voids. The structure aligns with the topological design shown in Fig. 1c. Notably, this scalable system requires no additional chemicals and is highly reproducible using standard laboratory procedures.

To test the device, two graphite current collectors were attached to both sides of the MEU (Fig. 4a). The cell underwent standard electrochemical tests within a 2.1 V voltage window (see Methods) to evaluate charge-discharge cycles (Fig. 4b), current-voltage characteristics (Fig. 4c), and estimate capacitance, coulombic efficiency, and energy efficiency. Despite its simple design (Fig. 4d) and use of pure water without additives, the cell showed impressive parameters and durability with no visible degradation after 60,000 cycles (Fig. 4e). This cycle life translates to over 150 years of operation counting one charge-discharge cycle per day, e.g., in the case of use with solar panels. It retains and releases energy with up to 100% coulombic and 60% energy efficiency, due to the absence of side reactions. The initial "annealing" period was assigned to the electric-field-stimulated wetting of nanopores.

Moreover, we found that the device has an electrolysis threshold of 1.65 V (Fig. 4f, and Fig. S11), higher than the standard 1.23-V limit for bulk water at neutral conditions, which yields higher capacitance, and energy density than that in bulk water systems. This is likely due to the combined effects of high water purity and the

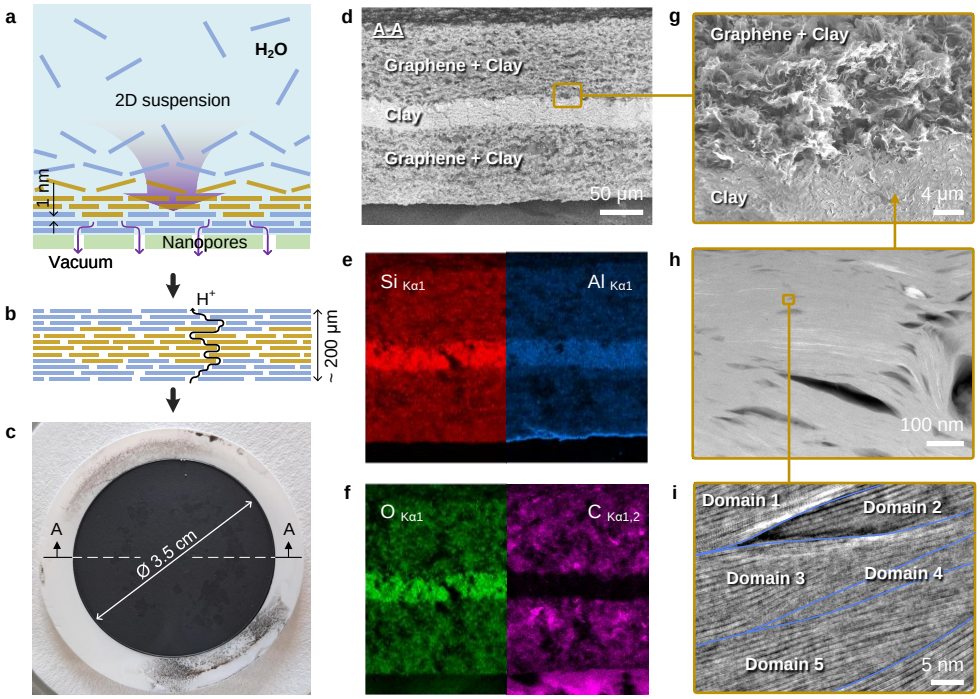

Fig. 3 'Blue battery' design and structure. (**a**) Schematic illustration of the wet assembling process to make the membrane electrode unit (MEU) via vacuum filtration through a nanoporous substrate. (**b**) Illustration of the self-assembly result: a vdW heterostructure with clay sandwiched between two graphene layers. Ultraconfined water is a continuous network—electrolyte. The arrow shows a pathway of H^+ ions during charge. (**c**) Photograph of the resulting three-layer MEU. (**d**) Scanning electron microscope (SEM) image of the MEU cross-section. (**e-f**) SEM energy dispersive X-ray (EDX) element mapping of the same MEU cross-section. The color maps of Si, Al, O, and C elements are displayed in red, blue, green, and magenta, respectively. For more data see SI Figs. S9, S10. (**g**) Enlarged SEM image of the electrode-separator border showing their mutual penetration without voids. (**h**) Annular dark-field (ADF) STEM image of a cross-section of the separator. (**i**) Enlarged iDPC STEM image of the domain intercalation after self-assembling. The blue lines are the guide for the eye.

ultraconfinement of water, which alters its electrodynamics, particularly conductivity (Fig. 2f) and polarizability [18, 19, 21]. Our system achieves a capacitance of around 40 F/g and an energy density of around 10 Wh/kg of electrode material, comparable to that of commercial supercapacitors [43]. Both parameters have the potential for further improvement through optimization.

Note that the device's efficiency and energy density significantly exceed those of biological systems such as photosynthesis, which has an efficiency below 1% [44]. Thus, our device mimics, but also surpasses nature. It traps and transports protons and hydroxides (proton holes) of the nanometer-thick water-solid interface within the cell over macroscopic distances in an external electric field and stores them in the same-size nanopores in the electrodes (see Fig. 1e). This effect is universal and can be used

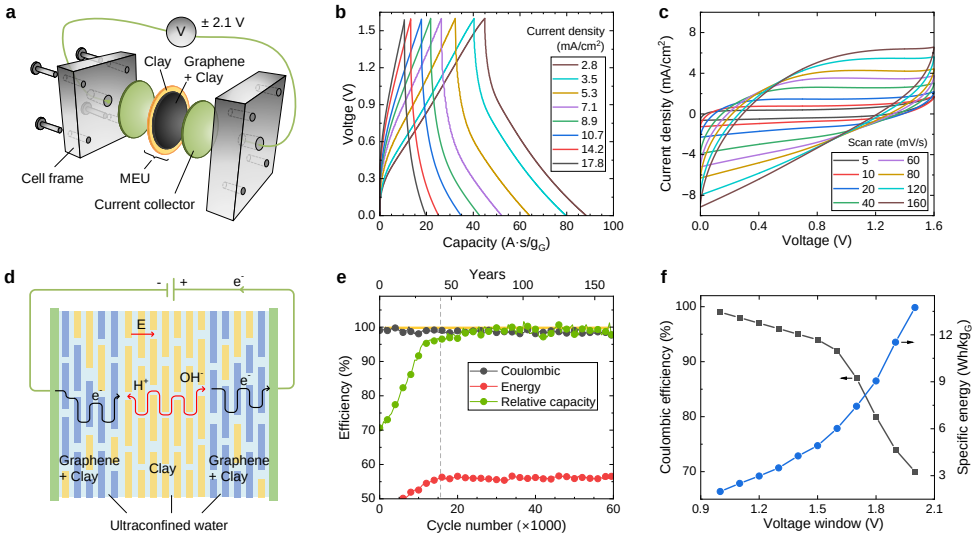

Fig. 4 'Blue battery' characteristics and working principle. (**a**) Schematic illustration of the measurement cell used in this study. (**b**) Charge-discharge plots at different current densities. (**c**) Cycling voltammograms at different scan rates. (**d**) Schematic illustration of the charge separation and storage mechanism. Strong 2D confinement stimulates proton transport within ultraconfined water. Proton (H^+) and hydroxides (OH^-, proton holes) accumulate on the opposite electrodes in the electrical double layers. The arrows schematically show the trajectory pass for electrons and ions. (**e**) Capacity retention, coulomb, and energy efficiency at long-term cycling for the voltage window of 0-1.6 V and the current of 10 mA. The initial part before the vertical dashed line is the system "annealing". The top scale is an equivalent cycle life in case it is used as a stationary backup in combination with wind generators and/or solar panels. (**f**) Coulombic efficiency and the device's energy density on the voltage window at the current of 8 mA.

in other types of electrochemical systems, such as electrolyzers, batteries, and fuel cells, as well as nature-signaling mimicking systems and neuromorphic devices.

2 Discussion

We have demonstrated a scalable platform for energy applications that leverages the anomalous properties of ultraconfined water: an enhanced proton conductivity [20] and heterogeneous polarizability [21]. The system is topologically non-equivalent to the standard electrochemical systems design (Fig. 1, a to c) and mimics nature's use of ultraconfinement and space (Fig. 1d). Our device, made from only abundant materials: graphene, clay, and water confined within 1-nm slit pores, serves as a rechargeable electricity retention unit with a projected lifespan of over 150 years (Fig. 4e). This makes it ideal for supplementing solar or wind generators to avoid grid instability, which is an urgent problem of a fast-growing renewable energy network. The exceptional durability and infinite materials sourcing suggest it could be a reliable solution for balancing electricity generation-consumption time lags or providing fast-frequency

control in the grid [45]. A performance comparison with current batteries and supercapacitors indicates that our system could offer superior long-term stability that suggests specific niche applications (SI Table S3).

Note that while using rare elements in energy devices can enhance reaction speed, energy density, efficiency, and operational ranges (voltage or temperature), our nature-mimicking approach suggests advantages in terms of cost, environmental safety, geopolitical stability, biocompatibility, scalability, structural stability, and durability. The non-toxic nature of clay [46] makes our platform also suitable for a range of bio-applications, including battery pills [47], bio-interfaces [6], neuromorphic computing [7], and even for use in Mars colonization, where clays and water are available on-site [48], whereas ultraconfined water does not freeze down to -70 °C [49].

In conclusion, our blue-battery platform represents a significant advance in applying nature-inspired principles to sustainable nanoengineering of energy systems. By combining 2D materials science with abundant materials and simple fabrication, we achieve high performance, safety, material independence, and sustainability. Our technology aims to drive further research and seek sustainable industrial applications, promoting a more efficient, environmentally friendly, and safer energy future.

3 Methods

3.1 Sample preparation

Several clay types: bentonite, montmorillonite, illite, kaolinite, and silt, were purchased from Merck and Nagra in the form of powder and grains. The samples were preliminary milled to the sub-micron sizes. Then, clay samples were washed out through a multi-step cleaning process involving repeated dissolution, natural sedimentation preselection, washing and centrifugation cycles, dialysis, and sonication, with zero chemicals used. The resulting product was a nonprecipitating colloidal solution of clay nanoparticles in distilled water with a concentration of about 0.1 mg/ml, a bulk electrical resistivity of approximately 18 MΩ, and a pH of 7. An electrochemically exfoliated graphene solution in distilled water was purchased from XFNano and used as received. Milli-Q water, with an 18 MΩ resistivity, served as the water source. Polymer-filter substrates with nanopores ranging from 20 to 100 nm were purchased from Merck and used without further modification.

3.2 Vacuum filtration

Clay films and devices were fabricated using vacuum filtration of colloidal graphene and pre-treated clay solutions through the nanopore polymer-filter-substrate vacuum filtration. Before use, all solutions were sonicated at 1200 Watts and 20-25 kHz and naturally thermally equilibrated with the lab temperature. For electrode fabrication, either a pure graphene solution or a clay-graphene suspension mixture was used (see SI Table S2 for different MEU compositions). A pure clay solution was utilized for the separator. To create the three-layer electrode-separator-electrode structure, the electrode solution, separator solution, and second electrode solution were sequentially filtered. A water vacuum pump facilitated water transport through the filter, and

filtration proceeded step-by-step, waiting for the complete passage of water from the previous step. Conductivity and pH tests of the filtrate confirmed no contamination.

Unlike pressing dry powders, vacuum filtration produces highly dense samples without large pores, featuring unidirectionally oriented "brick-and-mortar" structure layers of 2D materials held together by vdW forces. This method ensures remarkable mechanical stability, flexibility, and reproducibility for each membrane-electrode assembly.

3.3 Electrochemical measurements

Vacuum-filtrated samples were placed in a saturated water vapor atmosphere for 48 hours, with water saturation confirmed by mass gain and swelling checks, ensuring no contamination by foreign ionic or molecular species. Conductivity, charge-discharge (CD), cyclic voltammetry (CV), and long-term CD tests were conducted using the BioLogic SP-300 and CH Instruments devices. The voltage window was set to ± 2.1 V for preliminary tests and to ± 1.6 V for main measurements, including long-term stability tests. The second value was chosen according to the electrolysis limit observed via a hydrogen-evolution-reaction (HER) indicator in CV and CD curves (SI Fig. S11). Two graphite current collectors were applied to the electrodes in all measurements. To prevent water evaporation, Parafilm was used to seal the membrane-electrode unit. Notably, no mass change in the samples was detected over one month after the fabrication. Pressure applied to the current collectors was controlled by a custom-made sample holder and was adjusted to ensure good electrical contact.

3.4 X-ray diffraction measurement

X-ray diffraction (XRD) measurements were conducted using a Bruker D8 Discover in Bragg Brentano geometry, with a Kalpha1 - monochromated beam ($\lambda = 1.5406$ $\mathring{A}$) and a Lynxeye-XE detector and at the P62 SAXS/WAXS beamline of PETRA III synchrotron facility at Deutsches Elektronen-Synchrotron (DESY). We prepared two types of samples for these measurements: clay vacuum-filtered membranes and powders. For the Bruker measurements, dry samples were prepared by vacuum annealing for 24 hours, while wet samples were prepared by exposure to saturated water vapor for 48 hours. At PETRA III, the dry samples were similarly annealed, but the wet samples were prepared by directly adding water to the powders. The crystalline interlayer distance change on water adding (swelling effect) was found in both the PETRA III and lab-based XRD measurements (SI Fig. S7).

3.5 Scanning electron microscopy

Scanning electron microscopy (SEM) observation including EDX (energy dispersive X-ray spectroscopy) measurements was performed on an SEM/FIB (focused ion beam) Zeiss CrossBeam 550 microscope equipped with Oxford Instruments Ultim Max detector. SEM images were taken with 5 kV (Figs. S21, S22) and 3 kV (Figs. S23) accelerating voltage, while EDX data measurements were done at 15 kV (Figs. 3, d to g, and Figs. S9, S10). For subsequent transmission electron microscopy observation, a

lamella from a smectite membrane (Figs. S24, S25) was prepared using the SEM/FIB tool Zeiss NVision 40 using an accelerated Ga^+ beam at 30 kV and 5 kV.

3.6 Scanning transmission electron microscopy

Scanning transmission electron microscopy (STEM) experiments were realized on an aberration-corrected FEI Titan Themis^3 microscope operated at 300 kV. An electron probe of an 8 mrad half-convergence angle was used in association with a current of 10 pA. A dwell time of 2 µs was used for STEM imaging, which limited the total electron dose deposited on the sample for acquiring atomic-resolution STEM images to 460 $e^-/\mathring{A}^2$. Annular dark-field (ADF) and integrated differential phase contrast (iDPC) STEM images were collected simultaneously, using a collection angle ranging from 17 to 104 mrad for ADF and from 4 to 15 mrad for iDPC. iDPC STEM imaging allowed us to visualize the atomic structure of the crystal composed of light elements [50], with the moderate electron dose used to avoid degradation of the crystal structure during imaging.

4 Acknowledgements

We thank Keith Stevenson, Nianduo Cai, Artem Pronin, Maria Nieves López Salas, and Anton Andreev for fruitful discussions, Sylvio Haas (DESY) for help during the synchrotron radiation-based X-ray scattering experiments, Vytautas Navikas for the help with the representation of Figure 1e, and Milad Sabzehparvar for assistance in the lab. We also acknowledge the scientific exchange and support of the Centre for Molecular Water Science, and the research initiative BlueMat: Water-Driven Materials, Hamburg (Germany). We thank the EPFL Center for Electron Microscopy (CIME) for access to electron microscopes.

Funding

Y.T. acknowledges the financial support from the Swiss National Science Foundation through the National Centre of Competence in Research Bio-Inspired Materials and Grant No. 200021-192037. A.Ra. and T.H.C. acknowledge funding from the European Research Council (grant 101020445—2D-LIQUID). S.B. and L.L. are grateful for the financial support provided by the Swiss National Science Foundation (grant No. 200021-204099, Division II). Funding by the Deutsche Forschungsgemeinschaft (DFG, German Research Foundation) in the DFG Graduate School GRK 2462 'Processes in natural and technical Particle-Fluid-Systems (PintPFS)' (Project No. 390794421) is gratefully acknowledged. G.T. acknowledges support from the SNSF Eccellenza Grant 194181 and the SNSF Starting Grant 211695

Declarations

There are no conflicts of interest to declare. All data is available within this paper and Supplementary Information.

Author contribution

V.A. proposed and directed the research with the help of F.B., A.Ra., G.T., and L.L.; S.B. prepared the clay materials and characterized their optical, transport, and electrical properties together with V.A. and under the supervision of L.L.; Y.T. developed the vacuum filtration protocol and assembled the membranes and membrane-electrode units with V.A.; J.M. and V.A. conducted the electrochemical measurement under the guidance of G.T.; A.Ry. carried out the data analysis; T.-H.C. develop the protocol and processed the raw materials, controlled their purity, and measured ζ-potentials; L.N., V.B., and Y.T. conducted electron microscopy characterization; P.S. conducted X-ray diffraction experiments; M.L. and P.H. conducted synchrotron radiation-based X-ray scattering experiments and analyzed the data; V.A. wrote the manuscript; and all authors contributed to discussions.

References

[1] Eder, M., Amini, S., Fratzl, P.: Biological composites-complex structures for functional diversity. Science **362**, 543–547 (2018) https://doi.org/10.1126/science.aat8297

[2] Dargaville, B.L., Hutmacher, D.W.: Water as the often neglected medium at the interface between materials and biology. Nature Communications **13**, 4222 (2022) https://doi.org/10.1038/s41467-022-31889-x

[3] Lavine, M.S., Hines, P.J., McCartney, M., Ray, L.B., Hurtley, S.M., Ash, C., Smith, K.T.: Editors' choice. Science **371**, 1329–1330 (2021) https://doi.org/10.1126/science.2021.371.6536.twil

[4] Preston, F.W.: The commonness, and rarity, of species. Ecology **29**, 254–283 (1948) https://doi.org/10.2307/1930989

[5] Degen, F., Winter, M., Bendig, D., Tübke, J.: Energy consumption of current and future production of lithium-ion and post lithium-ion battery cells. Nature Energy **8**(11), 1284–1295 (2023) https://doi.org/10.1038/s41560-023-01355-z

[6] Shu, T., Herrera-Arcos, G., Taylor, C.R., Herr, H.M.: Mechanoneural interfaces for bionic integration. Nature Reviews Bioengineering **2**(5), 374–391 (2024) https://doi.org/10.1038/s44222-024-00151-y

[7] Marković, D., Mizrahi, A., Querlioz, D., Grollier, J.: Physics for neuromorphic computing. Nature Reviews Physics **2**(9), 499–510 (2020) https://doi.org/10.1038/s42254-020-0208-2

[8] Litman, Y., Chiang, K.-Y., Seki, T., Nagata, Y., Bonn, M.: Surface stratification determines the interfacial water structure of simple electrolyte solutions. Nature Chemistry **16**, 644–650 (2024) https://doi.org/10.1038/s41557-023-01416-6

[9] Banuelos, J.L., Borguet, E., Brown Jr, G.E., Cygan, R.T., DeYoreo, J.J., Dove, P.M., Gaigeot, M.P., Geiger, F.M., Gibbs, J.M., Grassian, V.H., Ilgen, A.G., Jun, Y.S., Kabengi, N., Katz, L., Kubicki, J.D., Lutzenkirchen, J., Putnis, C.V., Remsing, R.C., Rosso, K.M., Rother, G., Sulpizi, M., Villalobos, M., Zhang, H.: Oxide- and silicate-water interfaces and their roles in technology and the environment. Chemical Reviews **123**, 6413–6544 (2023) https://doi.org/10.1021/acs.chemrev.2c00130

[10] Dallin, B.C., Kelkar, A.S., Van Lehn, R.C.: Structural features of interfacial water predict the hydrophobicity of chemically heterogeneous surfaces. Chemical Science **14**, 1308–1319 (2023) https://doi.org/10.1039/D2SC02856E

[11] Rego, N.B., Ferguson, A.L., Patel, A.J.: Learning the relationship between nanoscale chemical patterning and hydrophobicity. Proceedings of the National Academy of Sciences **119**, 2200018119 (2022) https://doi.org/10.1073/pnas.2200018119

[12] Le Donne, A., Tinti, A., Amayuelas, E., Kashyap, H.K., Camisasca, G., Remsing, R.C., Roth, R., Grosu, Y., Meloni, S.: Intrusion and extrusion of liquids in highly confining media: bridging fundamental research to applications. Advances in Physics: X **7**, 2052353 (2022) https://doi.org/10.1080/23746149.2022.2052353

[13] Chaillet, M.L., Lengauer, F., Adolphs, J., Müh, F., Fokas, A.S., Cole, D.J., Chin, A.W., Renger, T.: Static disorder in excitation energies of the fenna-matthews-olson protein: Structure-based theory meets experiment. The Journal of Physical Chemistry Letters **11**, 10306–10314 (2020) https://doi.org/10.1021/acs.jpclett.0c02811

[14] Corti, H.R., Appignanesi, G.A., Barbosa, M.C., Bordin, J.R., Calero, C., Camisasca, G., Elola, M.D., Franzese, G., Gallo, P., Hassanali, A., Huang, K., Laria, D., Menéndez, C.A., Oca, J.M.M., Longinotti, M.P., Rodriguez, J., Rovere, M., Scherlis, D., Szleifer, I.: Structure and dynamics of nanoconfined water and aqueous solutions. The European Physical Journal E **44**, 136 (2021) https://doi.org/10.1140/epje/s10189-021-00136-4

[15] Cerveny, S., Mallamace, F., Swenson, J., Vogel, M., Xu, L.: Confined water as model of supercooled water. Chemical Reviews **116**, 7608–7625 (2016) https://doi.org/10.1021/acs.chemrev.5b00609

[16] Muñoz-Santiburcio, D., Marx, D.: Chemistry in nanoconfined water. Chemical Science **12**, 2931–2941 (2021) https://doi.org/10.1039/C6SC04989C

[17] Artemov, V.: The Electrodynamics of Water and Ice. Springer, Cham (2021)

[18] Artemov, V.G.: Dynamical conductivity of confined water. Measurement Science and Technology **28**, 014013 (2017) https://doi.org/10.1088/1361-6501/28/1/014013

[19] Fumagalli, L., Esfandiar, A., Fabregas, R., Hu, S., Ares, P., Janardanan, A., Yang, Q., Radha, B., Taniguchi, T., Watanabe, K., Gomila, G., Novoselov, K.S., Geim, A.K.: Anomalously low dielectric constant of confined water. Science **360**, 1339–1342 (2018) https://doi.org/10.1126/science.aat4191

[20] Artemov, V.G., Uykur, E., Kapralov, P.O., Kiselev, A., Stevenson, K.J., Ouerdane, H., Dressel, M.: Anomalously high proton conduction of interfacial water. J. Phys. Chem. Lett. **11**, 3623–3628 (2020) https://doi.org/10.1021/acs.jpclett.0c00910

[21] Wang, R., Souilamas, M., Esfandiar, A., Fabregas, R., Benaglia, S., Nevison-Andrews, H., Yang, Q., Normansell, J., Ares, P., Ferrari, G., Principi, A., Geim, A.K., Fumagalli, L.: In-plane dielectric constant and conductivity of confined water. arXiv preprint **2407.21538** (2024) https://doi.org/10.48550/arXiv.2407.21538

[22] Liang, Y., Yao, Y.: Designing modern aqueous batteries. Nature Reviews Materials **8**(2), 109–122 (2023) https://doi.org/10.1038/s41578-022-00511-3

[23] Wang, Y., Xia, Y.: Recent progress in supercapacitors: From materials design to system construction. Advanced Materials **25**(37), 5336–5342 (2013) https://doi.org/10.1002/adma.201301932

[24] Siria, A., Poncharal, P., Biance, A.L., Fulcrand, R., Blase, X., Purcell, S.T., Bocquet, L.: Giant osmotic energy conversion measured in a single transmembrane boron nitride nanotube. Nature **494**, 455–458 (2013) https://doi.org/10.1038/nature11876

[25] Melnik, S., Ryzhov, A., Kiselev, A., Radenovic, A., Weil, T., Stevenson, K.J., Artemov, V.G.: Confinement-controlled water engenders unusually high electrochemical capacitance. The Journal of Physical Chemistry Letters **14**(29), 6572–6576 (2023) https://doi.org/10.1021/acs.jpclett.3c01498

[26] Wang, L., Wang, Z., Patel, S.K., Lin, S., Elimelech, M.: Nanopore-based power generation from salinity gradient: Why it is not viable. ACS Nano **15**, 4093–4107 (2021) https://doi.org/10.1021/acsnano.0c08628

[27] Aluru, N.R., Aydin, F., Bazant, M.Z., Blankschtein, D., Brozena, A.H., Souza, J.P., Elimelech, M., Faucher, S., Fourkas, J.T., Koman, V.B., Kuehne, M., Kulik, H.J., Li, H.-K., Li, Y., Li, Z., Majumdar, A., Martis, J., Misra, R.P., Noy, A., Pham, T.A., Qu, H., Rayabharam, A., Reed, M.A., Ritt, C.L., Schwegler, E., Siwy, Z., Strano, M.S., Wang, Y., Yao, Y.-C., Zhan, C.a., Zhang, Z.: Fluids and electrolytes under confinement in single-digit nanopores. Chemical Reviews **123**, 34331–4405 (2023) https://doi.org/10.1021/acs.chemrev.2c00155

[28] Cenaj, O., Allison, D.H.R., Imam, R., Zeck, B., Drohan, L.M., Chiriboga, L.,

Llewellyn, J., Liu, C.Z., Park, Y.N., Wells, R.G., Theise, N.D.: Evidence for continuity of interstitial spaces across tissue and organ boundaries in humans. Communications Biology **4**, 436 (2021) https://doi.org/10.1038/s42003-021-01962-0

[29] Schechner, S.: The art of making leyden jars and batteries according to benjamin franklin. eRittenhouse **26**, 1–11 (2015)

[30] Du, P., Yuan, P., Liu, J., Ye, B.: Clay minerals on mars: an up-to-date review with future perspectives. Earth-Science Reviews **243**, 104491 (2023) https://doi.org/10.1016/j.earscirev.2023.104491

[31] Mitchell, J.K., Soga, K.: Fundamentals of Soil Behavior (3rd Ed.). John Wiley and Sons, New Jersey (2005)

[32] Zou, Y.-C., Mogg, L., Clark, N., Bacaksiz, C., Milovanovic, S., Sreepal, V., Hao, G.-P., Wang, Y.-C., Hopkinson, D.G., Gorbachev, R., Shaw, S., Novoselov, K.S., Raveendran-Nair, R., Peeters, F.M., Lozada-Hidalgo, M., Haigh, S.J.: Ion exchange in atomically thin clays and micas. Nature Materials **20**, 1677–1682 (2021) https://doi.org/10.1038/s41563-021-01072-6

[33] Ito, A., Wagai, R.: Global distribution of clay-size minerals on land surface for biogeochemical and climatological studies. Scientific Data **4**, 170103 (2017) https://doi.org/10.1038/sdata.2017.103

[34] Yang, E.-H., Datta, D., Ding, J., Hader, G.E..: Synthesis, Modelling and Characterization of 2D Materials and Their Heterostructures. Elsevier, Philadelphia (2020)

[35] Wang, P., Jia, C., Huang, Y., Duan, X.: Van der Waals heterostructures by design: From 1d and 2d to 3d. Matter **4**, 382–423 (2021) https://doi.org/10.1016/j.matt.2020.12.015

[36] Plötze, M., Niemz, P.: Porosity and pore size distribution of different wood types as determined by mercury intrusion porosimetry. Eur. J. Wood Prod. **69**, 649–657 (2011) https://doi.org/10.1007/s00107-010-0504-0

[37] Bich, L., Pradeu, T., Moreau, J.F.: Understanding multicellularity: The functional organization of the intercellular space. Frontiers in Physiology **10**, 1170 (2019) https://doi.org/10.3389/fphys.2019.01170

[38] Geim, A.K., Grigorieva, I.V.: Van der Waals heterostructures. Nature **499**, 419–425 (2013) https://doi.org/10.1038/nature12385

[39] Norrish, K.: Crystalline swelling of montmorillonite: Manner of swelling of montmorillonite. Nature **173**, 256–257 (1954) https://doi.org/10.1038/173256a0

[40] Seiphoori, A., Ferrari, A., Laloui, L.: Water retention behaviour and microstructural evolutions of mx-80 granular bentonite during wetting and drying cycles. Geotechnique **64**, 1–14 (2014) https://doi.org/10.1680/geot.14.P.017

[41] Austen Angell, C., Ansari, Y., Zhao, Z.: Ionic liquids: Past, present and future. Faraday Discuss. **154**, 9–27 (2012) https://doi.org/10.1039/C1FD00112D

[42] Artemov, V.G., Volkov, A.A., Sysoev, N.N.: On autoionization and pH of liquid water. Doklady Physics **61**(1), 1–4 (2016) https://doi.org/10.1134/S1028335816010043

[43] Pathak, M., Bhatt, D., Bhatt, R.C., Bohra, B.S., Tatrari, G., Rana, S., Arya, M.C., Sahoo, N.G.: High energy density supercapacitors: An overview of efficient electrode materials, electrolytes, design, and fabrication. The Chemical Record **23**, 202300236 (2023) https://doi.org/10.1002/tcr.202300236

[44] Salimijazi, F., Parra, E., Barstow, B.: Electrical energy storage with engineered biological systems. Journal of Biological Engineering **13**, 38 (2019) https://doi.org/10.1186/s13036-019-0162-7

[45] Smith, O., Cattell, O., Farcot, E., O'Dea, R.D., Hopcraft, K.I.: The effect of renewable energy incorporation on power grid stability and resilience. Science Advances **8**, 6734 (2022) https://doi.org/10.1126/sciadv.abj6734

[46] Mousa, M., Evans, N.D., Oreffo, R.O., Dawson, J.I.: Clay nanoparticles for regenerative medicine and biomaterial design: A review of clay bioactivity. Biomaterials **159**, 204–214 (2018) https://doi.org/10.1016/j.biomaterials.2017.12.024

[47] Abdigazy, A., Arfan, M., Lazzi, G., Sideris, C., Abramson, A., Khan, Y.: End-to-end design of ingestible electronics. Nature Electronics **7**(2), 102–118 (2024) https://doi.org/10.1038/s41928-024-01122-2

[48] Ehlmann, B.L., Mustard, J.F., Murchie, S.L., Poulet, F., Bishop, J.L., Brown, A.J., Calvin, W.M., Clark, R.N., Des Marais, D.J., Milliken, R.E., Roach, L.H., Roush, T.L., Swayze, G.A., Wray, J.J.: Subsurface water and clay mineral formation during the early history of mars. Nature **479**, 53–60 (2011) https://doi.org/10.1038/nature10582

[49] Findenegg, G.H., Jähnert, S., Akcakayiran, D., Schreiber, A.: Freezing and melting of water confined in silica nanopores. ChemPhysChem **9**(18), 2651–2659 (2008) https://doi.org/10.1002/cphc.200800616

[50] Bosch, E.G.T., Lazic, I., Lazar, S.: Integrated differential phase contrast (iDPC) stem: A new atomic resolution stem technique to image all elements across the periodic table. Microscopy and Microanalysis **22**(S3), 306–307 (2016) https://doi.org/10.1017/S1431927616002385

Supporting Information

Ultraconfined 1-nm water as nature-inspired electrolyte for blue batteries

Vasily Artemov[1], Svetlana Babiy[2], Yunfei Teng[1,3], Jiaming Ma[4], Alexander Ryzhov[5], Tzu-Heng Chen[1], Lucie Navratilova[6], Victor Boureau[6], Pascal Schouwink[7], Mariia Liseanskaia[8], Patrick Huber[8,9], Fikile Brushett[10], Lyesse Laloui[2], Giulia Tagliabue[4], Aleksandra Radenovic[1,3]

[1]*Laboratory of Nanoscale Biology (LBEN), École polytechnique fédérale de Lausanne (EPFL), Lausanne, 1015, Switzerland.*

[2]*Soil Mechanics Laboratory (LMS), École polytechnique fédérale de Lausanne (EPFL), Lausanne, 1015, Switzerland.*

[3]*NCCR Bio-Inspired Materials, École polytechnique fédérale de Lausanne (EPFL), Lausanne, 1015, Switzerland.*

[4]*Laboratory of Nanoscience for Energy Technologies (LNET), École polytechnique fédérale de Lausanne (EPFL), Lausanne, 1015, Switzerland.*

[5]*Center for Transport Technologies, Austrian Institute of Technology (AIT), Vienna, 1210, Austria.*

[6]*Interdisciplinary Center for electron microscopy (CIME), École polytechnique fédérale de Lausanne (EPFL), Lausanne, 1015, Switzerland.*

[7]*X-ray Diffraction and Surface Analytics Platform (XRDSAP), École polytechnique fédérale de Lausanne (EPFL), Lausanne, 1015, Switzerland.*

[8]*Institute for Materials and X-ray Physics, Hamburg University of Technology (TUHH), Hamburg, 21073, Germany.*

[9]*Deutsches Elektronen-Synchrotron DESY, Hamburg, 22607, Germany.*

[10]*Department of Chemical Engineering, Massachusetts Institute of Technology (MIT), Cambridge, 02139, MA.*

This PDF file contains:

1. Supplementing figures
2. Battery characterization
3. Clay's electrical properties on compactness, clay type, and water content
4. SEM, TEM, and STEM images

Figures S1 to S26

Tables S1 to S3

References (1-3)

1. Supplementing figures

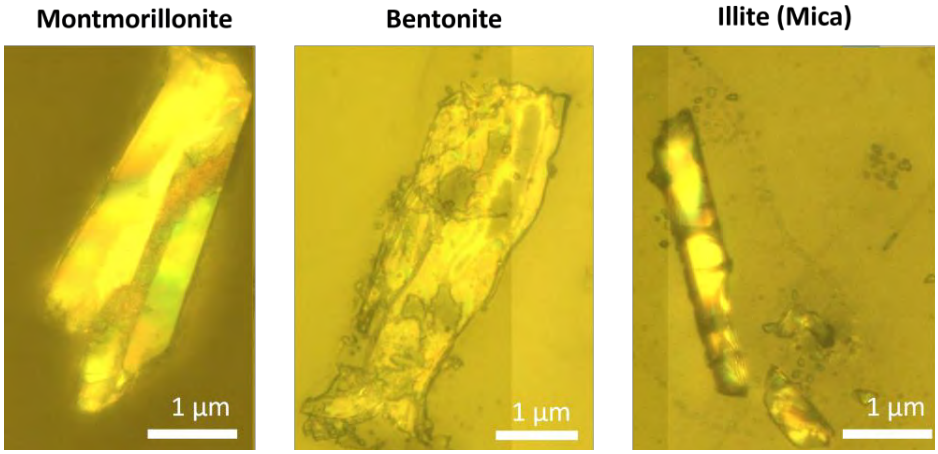

Fig. S1. Optical photos of large clay crystals of montmorillonite, bentonite, and illite, from left to right, respectively.

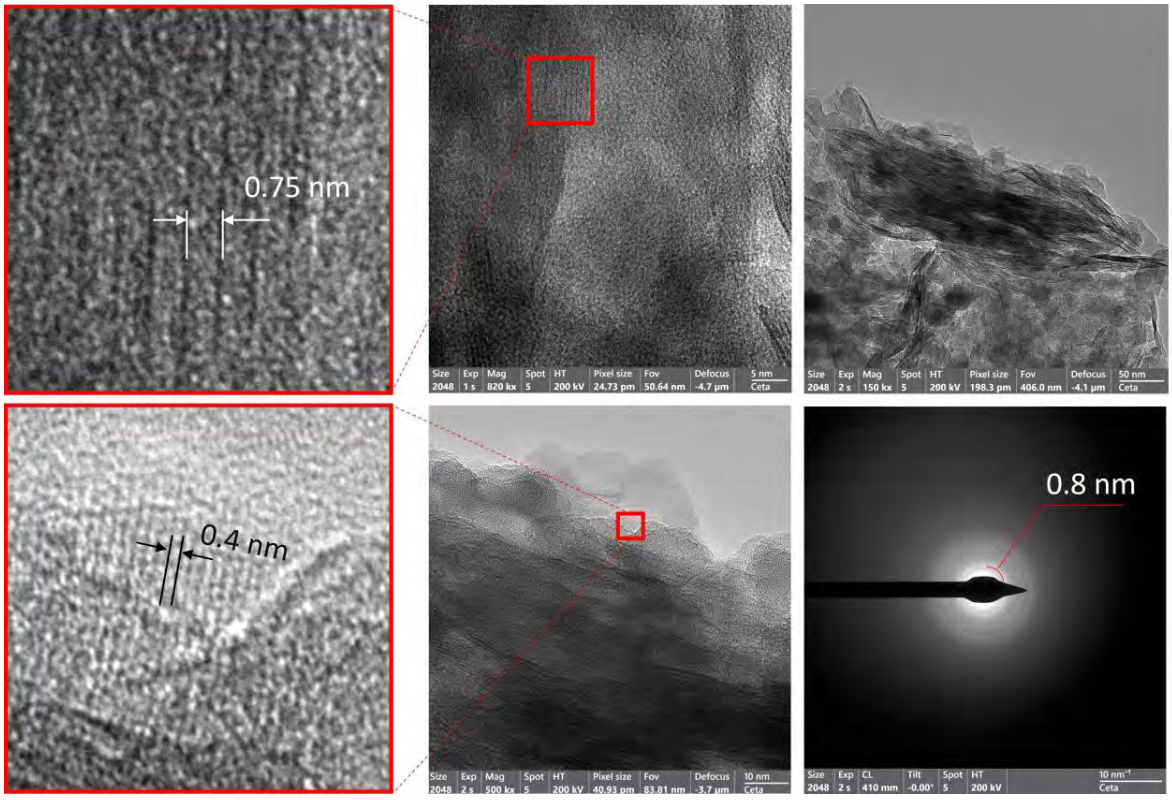

Fig. S2. Transmission electron microscopy (TEM) images and selected area electron diffraction (SAED) pattern of montmorillonite (MMT) crystals.

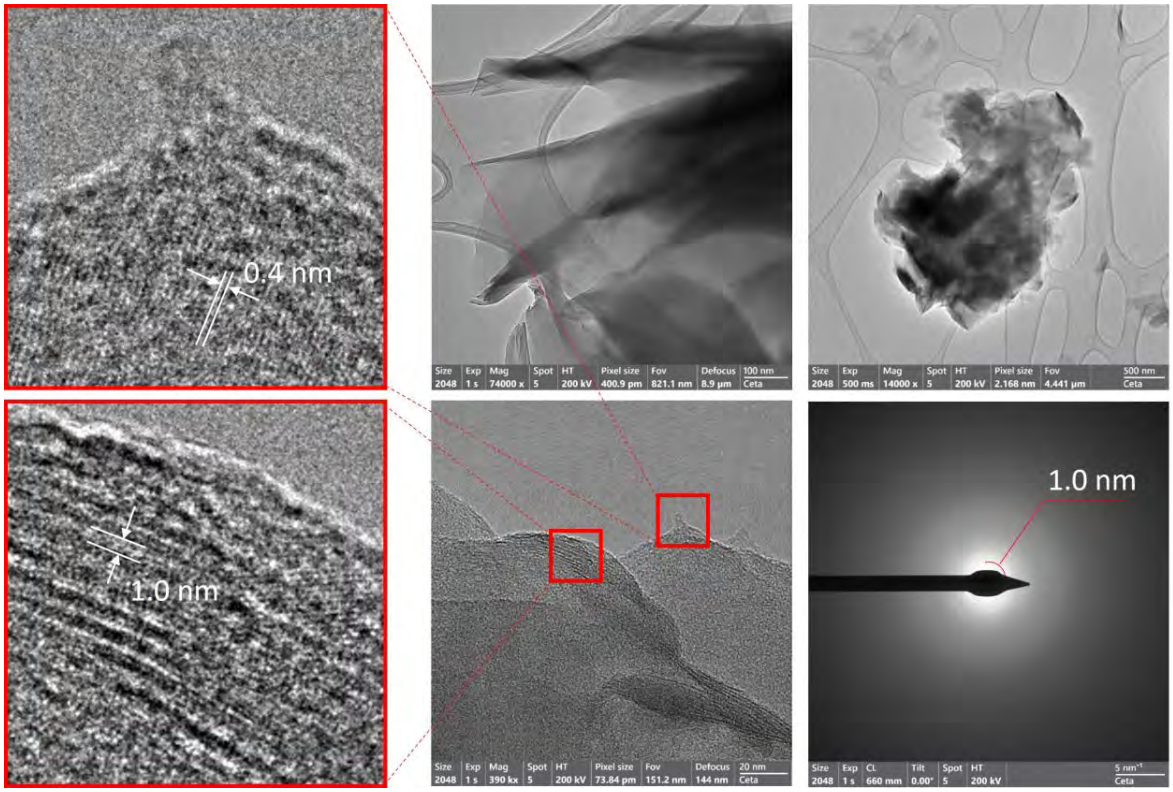

Fig. S3. The same as in Fig. S2 but for bentonite crystals.

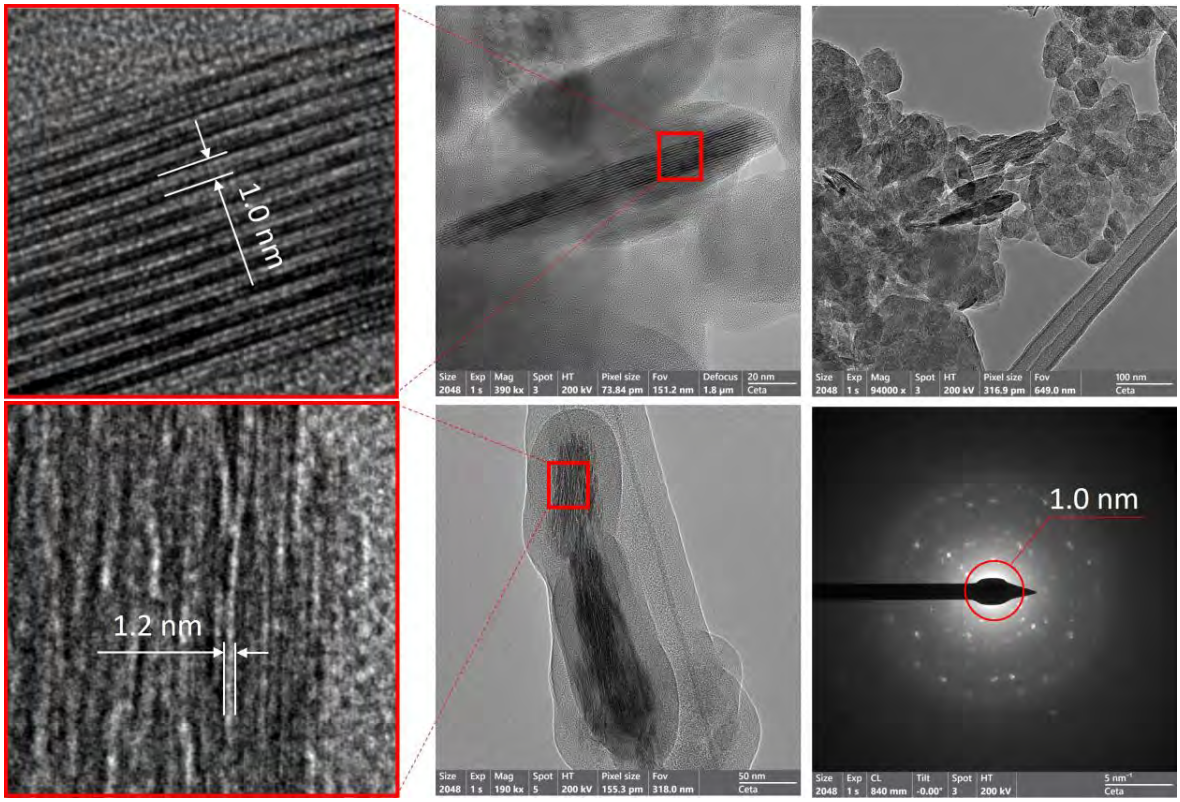

Fig. S4. The same as in Fig. S2 and S3 but for illite crystals.

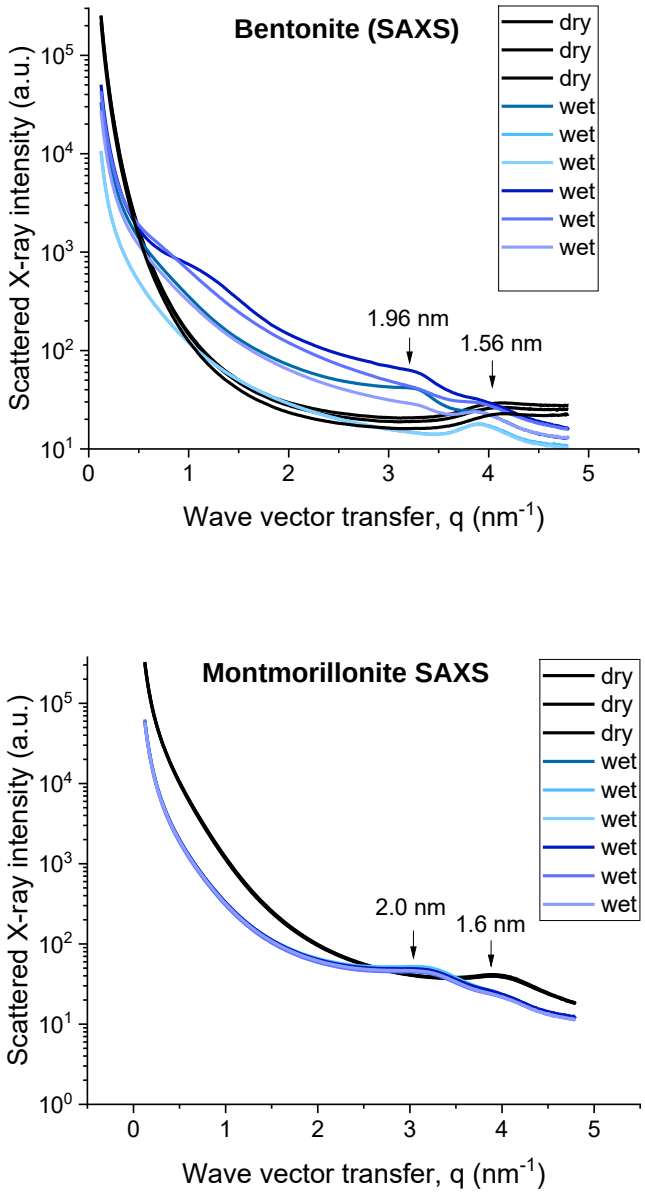

Fig. S5. Small-angle X-ray scattering (SAXS) of wet and dry bentonite (top) and montmorillonite (bottom) clay powders, recorded at the P62 SAXS/WAXS beamline of the PETRA III synchrotron source. The numbers next to the arrows indicate the interlayer distances corresponding to the peak maxima in reciprocal space. Note that the semi-dry sample was stored in a low-humidity environment without vacuum or annealing, resulting in a larger interlayer distance compared to the vacuum-dried TEM samples in Figs. S2–S4.

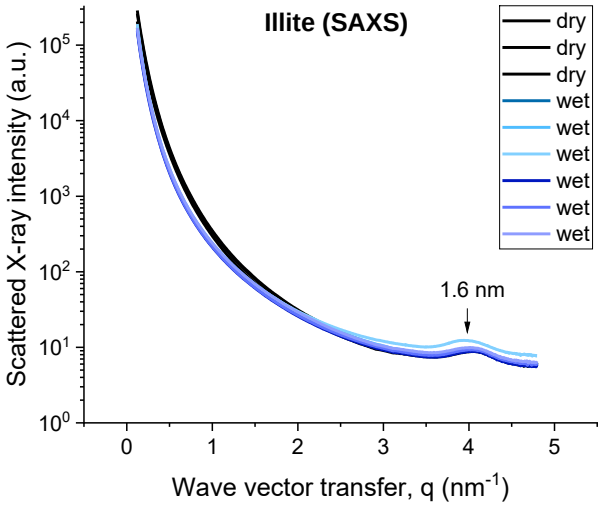

Fig. S6. Same as in Fig. S5 for illite clay powders. No diffraction peak shift indicates no water penetration between the crystalline layers (see Fig. 2c of the main text).

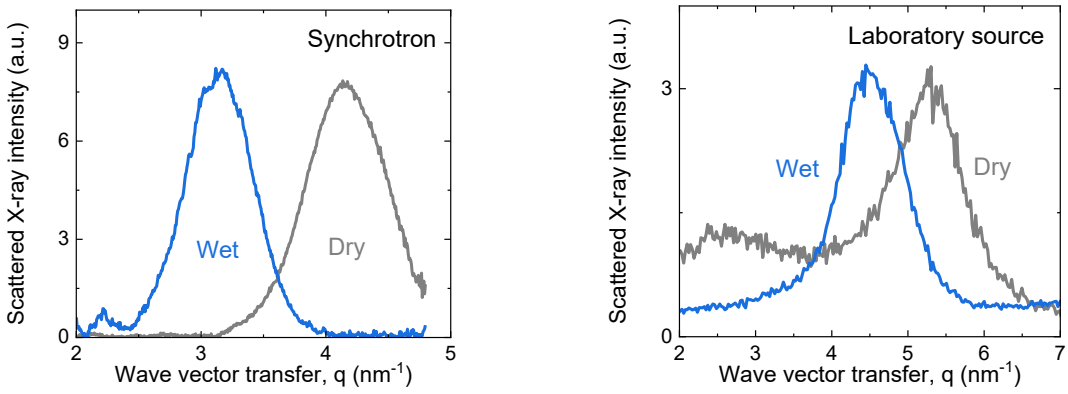

Fig. S7. Small-angle X-ray scattering (SAXS) of wet and dry bentonite clay powders. The data show the first diffraction peak. The graph on the left is synchrotron data (Fig. S5 with subtracted baseline). The samples were immersed in liquid water. The data on the right is Bruker XRD laboratory source measurements. The samples were prepared in saturated water vapor. The shift of the peaks in both measurements confirms water penetration between the bentonite clay crystal layers.

Table S1. ξ-potentials (in mV) of the nano-colloidal solutions of different clay types and graphene in pure 18-MΩ water with a pH of 7. Measurements were done with Malvern Panalytical™ Zetasizer.

Meas. number	Smectite (MMT)	Kaolinite	Illite	Graphene
1	-30.9	-17.2	-15.2	-16.2
2	-31.7	-16.4	-16.6	-15.5
3	-30.6	-16.7	-15.2	-14.9
Average	-31.1	-16.8	-15.7	-15.5

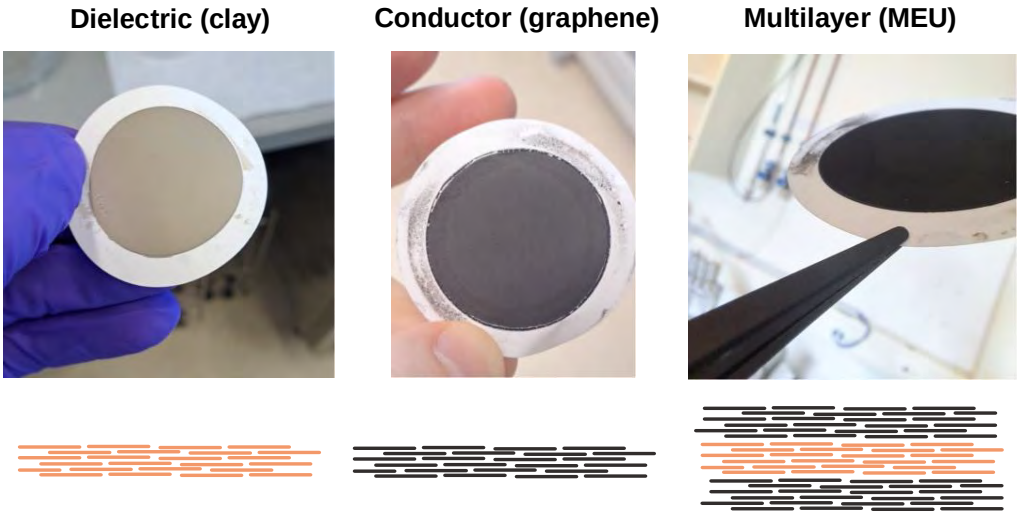

Fig. S8. Van der Waals heterostructures made in this study. Ø3.5-cm film membranes of clay (left), graphene (middle), and a multilayer graphene-clay-graphene membrane-electrode unit (MEU). The bottom sections schematically illustrate the structure of the films, where a stick represents a 2D crystal of the original material. These crystals are unidirectionally oriented and held together by van der Waals forces, providing enhanced flexibility and mechanical stability compared to compressed clay-based structures.

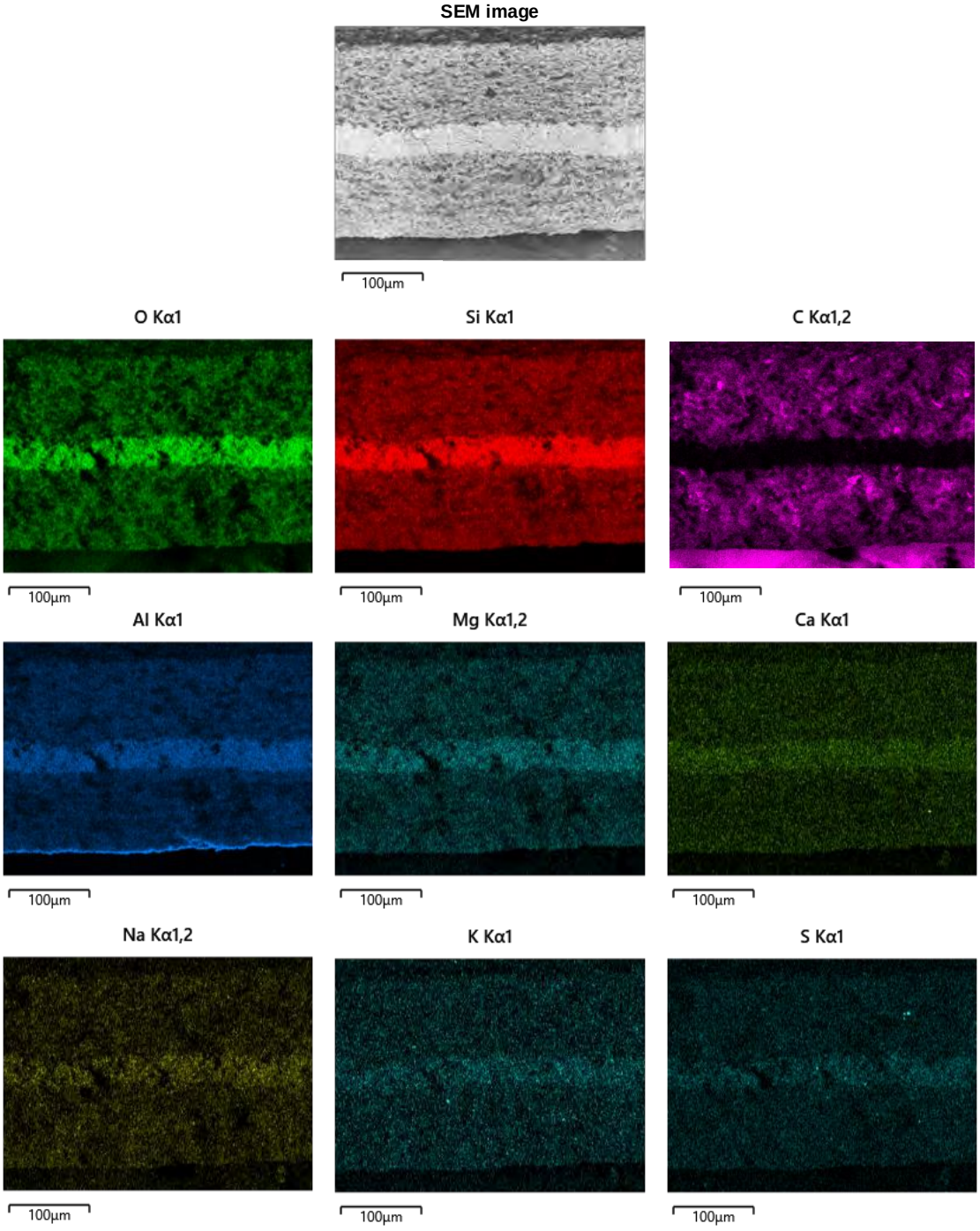

Fig. S9. SEM energy dispersive X-ray (EDX) element mapping for a cross-section of a membrane-electrode unit (MEU) made of smectite clay and graphene. Color maps are associated with the chemical species expected in the system (O, Si, C, Al, and Mg), in agreement with crystal structure, plus traces of Ca, Na, K, and S. The top is the SEM micrograph. The EDX sum spectrum of the element mapping is shown in Fig. S10.

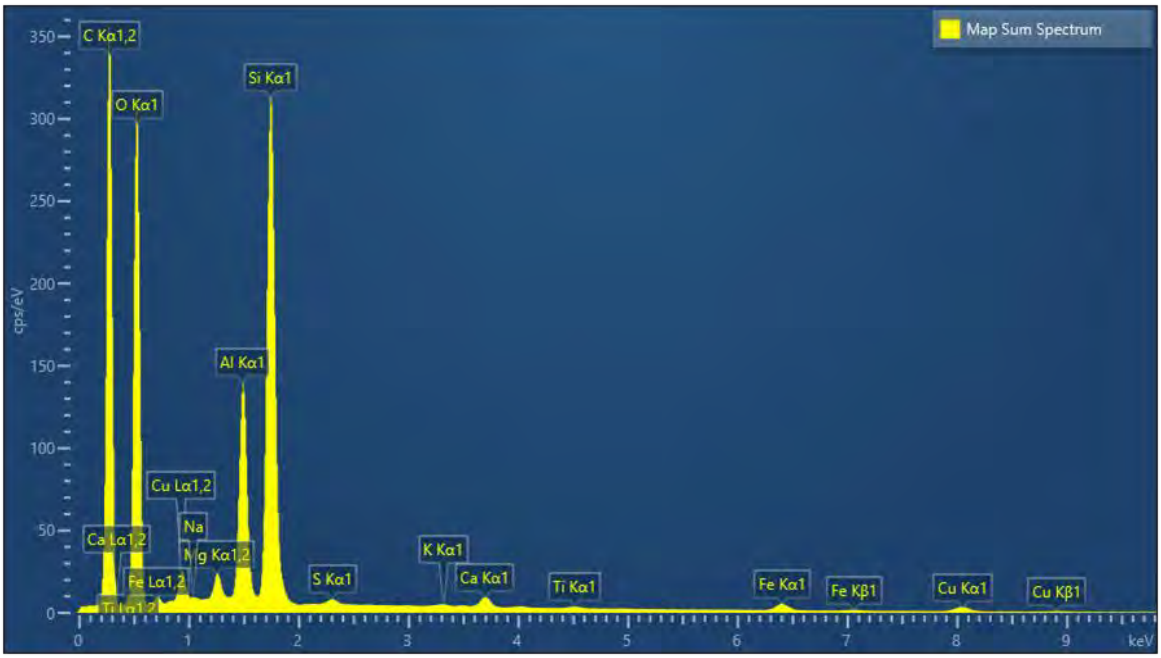

Fig. S10. EDX sum spectrum associated with the elemental map shown in Fig. S9. The spectrum indicated the presence of the chemical species composing the clay crystal structure, alone.

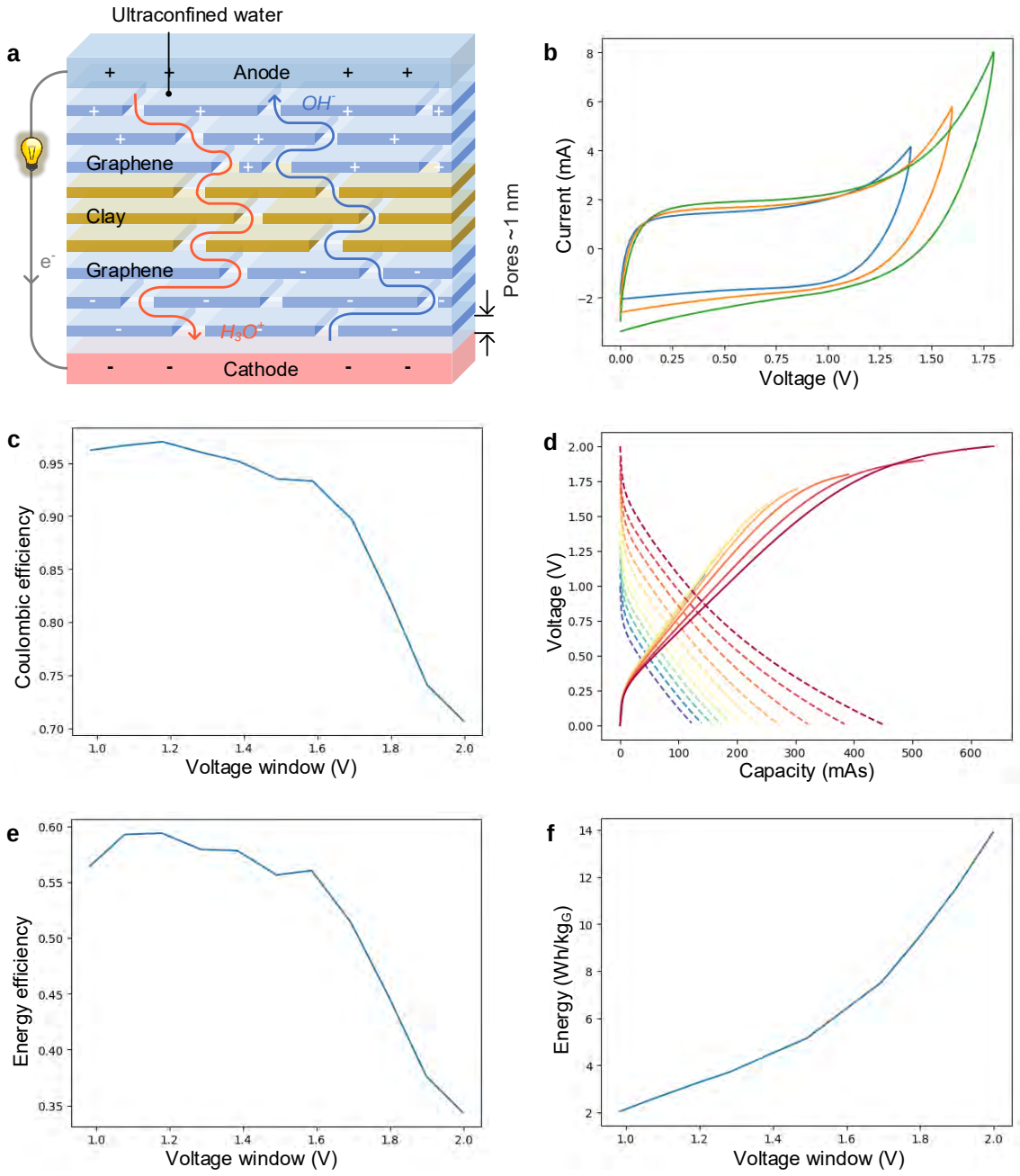

Fig. S11. Test for the hydrogen evolution reaction (HER). (a) Schematic representation of the blue battery cell. (b, d) Current-voltage characteristics and charge-discharge curves at different cut-off voltages. (c, e, f) Coulombic efficiency, energy efficiency, and specific energy of the cell as functions of the working voltage window. The trade-off voltage is around 1.65–1.70 V. The HER threshold is approximately 1.65 V, which is higher than the 1.23 V of bulk water.

2. Battery characterization

We characterized the cell using cyclic voltammetry (CV) and charge-discharge (CD) tests. In the CV measurements, the current was monitored while varying the voltage at a fixed rate. In contrast, during the CD tests, the voltage was adjusted while maintaining a constant current. CV measurements were employed to calculate the capacitance, *C*, using the following equation:

$$C = \frac{\int idv}{2\mu m \Delta V}, \tag{S1}$$

where *i* and *v* are the current and potential in the CV test, μ is the scan rate in V/s, m is the mass of active materials in grams, ΔV is the voltage (potential) window during discharge in V, *I* is the constant discharge current in A, and Δt is the discharge time in seconds. An example of the results can be seen in Fig. S12.

CD curves were used to calculate the energy density, E, using the formula:

$$E = \int_{DC} \frac{IUdt}{m}, \tag{S2}$$

and the power density, P, by:

$$P = \frac{E}{\Delta t}. \tag{S3}$$

An example of these results is provided in Fig. S13. The energy and coulombic efficiencies were determined from the CD and CV tests by dividing the output by the input energy and charge. These results are presented as percentages in Fig. S13. Finally, the long-term charge-discharge, and the self-discharge assessment test were performed. The results are given in Figs. S14 and S15.

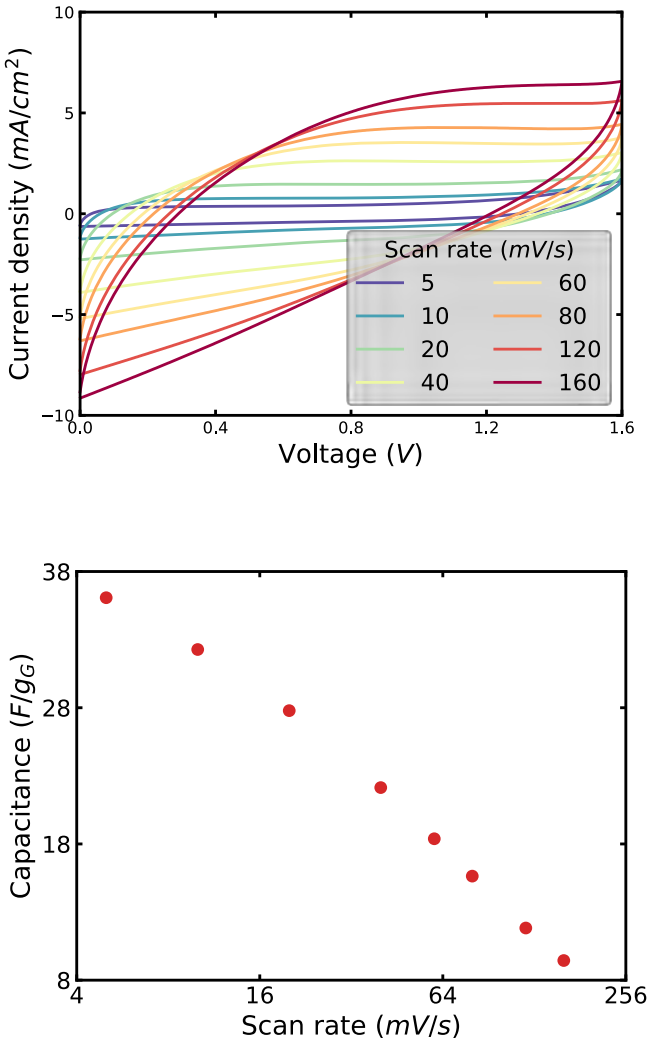

Fig. S12. Blue-battery cyclic voltammograms (top) and specific capacitance vs. scan rate, calculated according to Eq. (S1). The voltage window is $\Delta V = 1.6$ V.

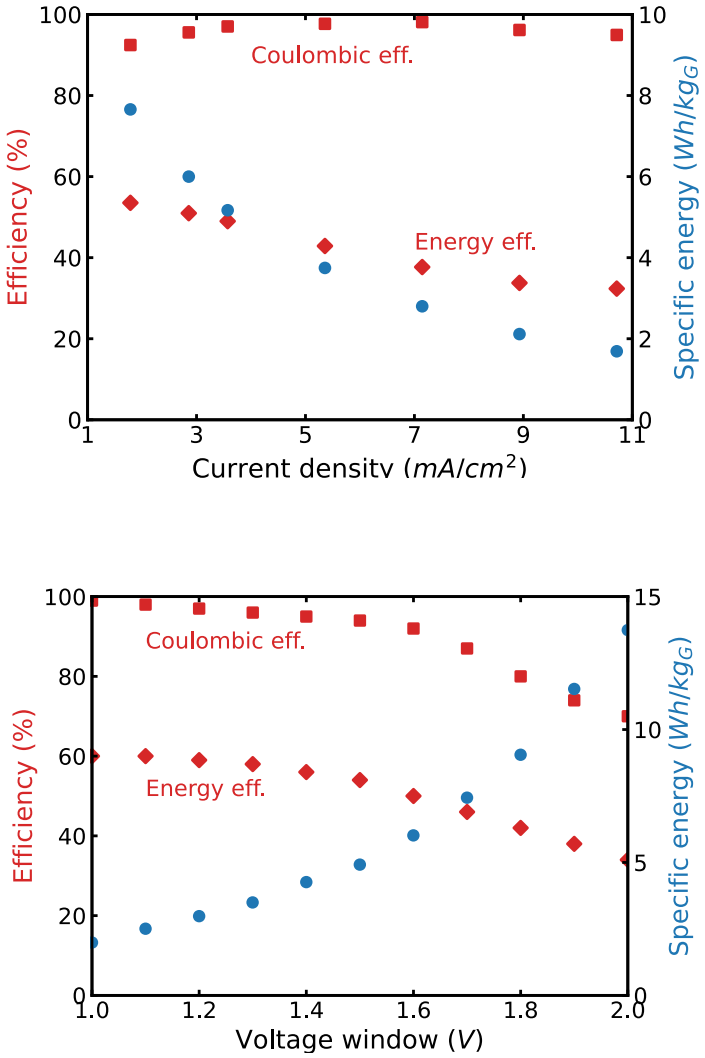

Fig. S13. Coulombic and energy efficiencies, as well as specific energy of the blue battery, at different current densities (top) and voltage windows (bottom).

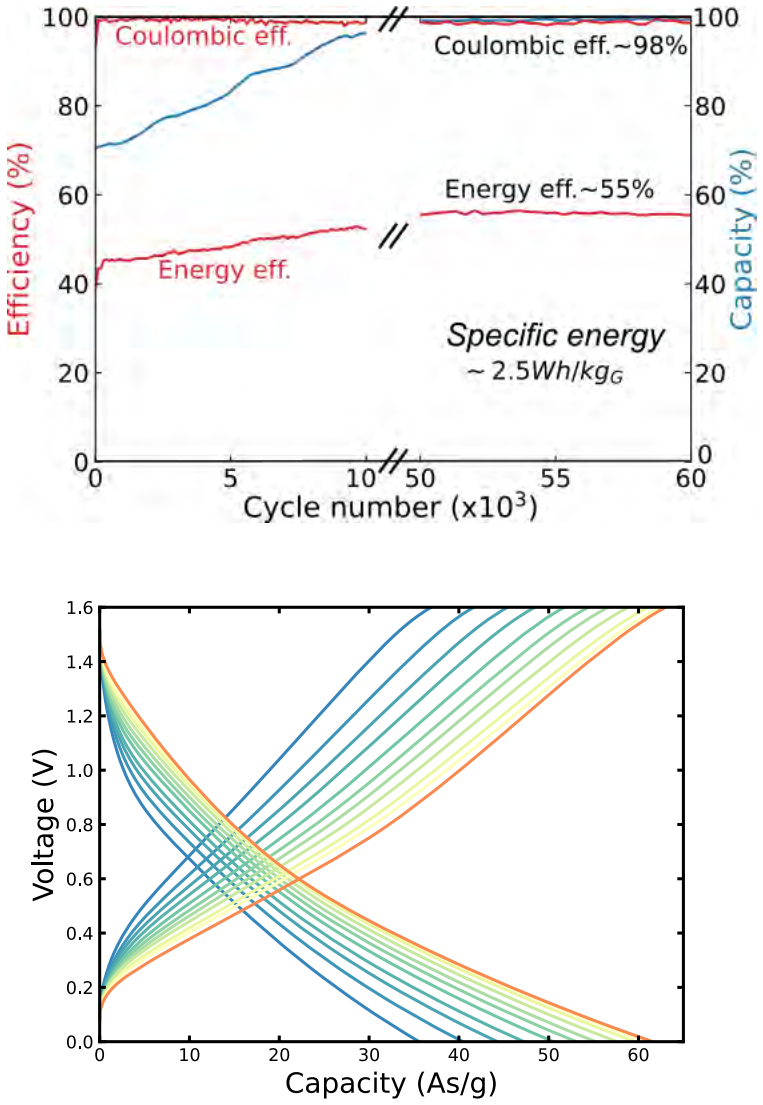

Fig. S14. Long-term stability test. The figure shows the evolution of the blue battery's efficiency, capacity, and specific energy over more than 60,000 cycles. The initial period exhibits an "annealing" effect, likely due to the electrowetting of nanopores. The bottom graph displays the progression of the charge-discharge curves, with blue representing the initial cycles and red representing the final cycles.

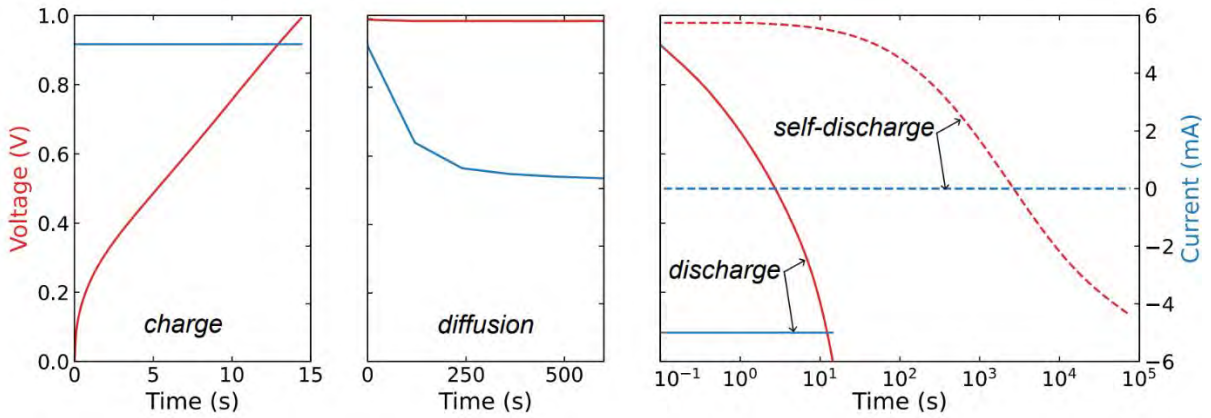

Fig. S15. Self-discharge assessment. The blue-battery charge phase with a fixed current (left), the diffusion phase with a variable current to maintain a constant voltage (middle), and the discharge phase (right), show both load discharge (solid line) and self-discharge with no load (dashed line). Note the logarithmic scale for the time in the right graph. The self-discharge occurs at a rate four orders of magnitude slower than the load discharge, indicating that the system is suitable for short- to mid-term electricity storage as a backup or an energy reserve, or a system where the fast charge-discharge and high power are needed, such as fast frequency control in the grid, or a regenerative brake system.

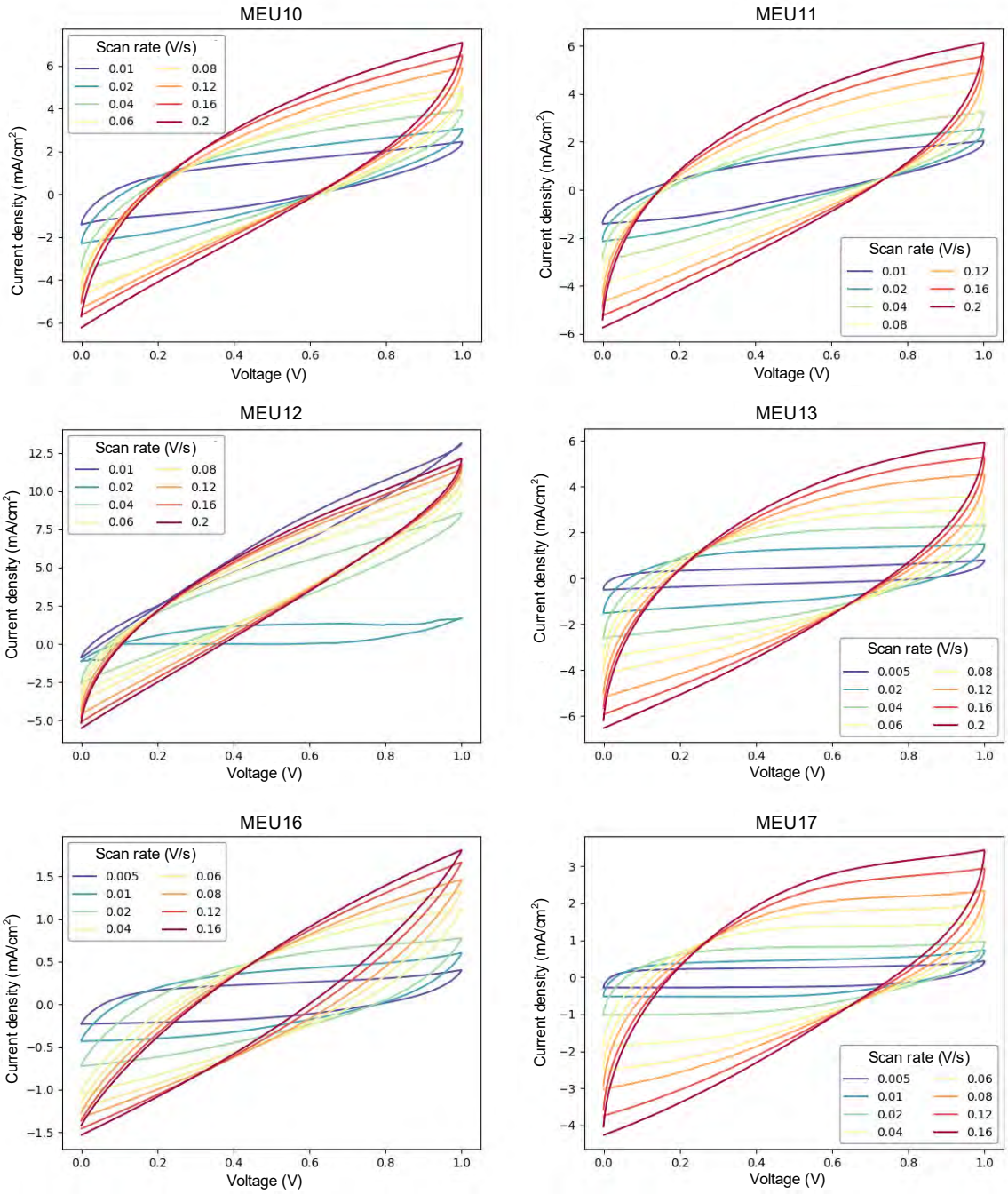

Fig. S16. Cyclic voltammograms for several different MEUs (see the number on top of the panels) at different scan rates. For MEU composition see Table 2.

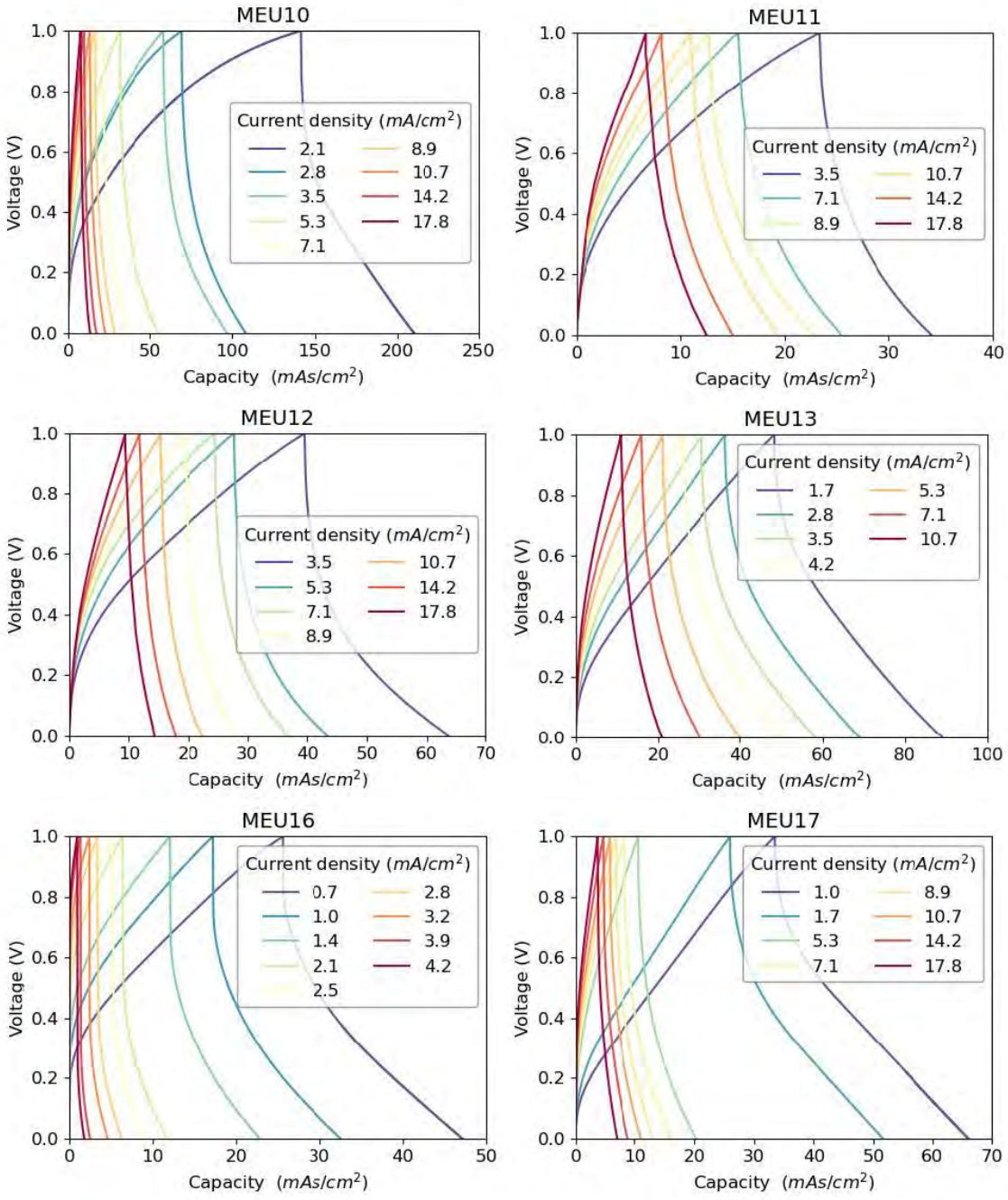

Fig. S17. Charge-discharge curves for several different MEUs (see the number on top of the panels) at different current densities. For MEU composition see Table 2.

Table S2. The list of membrane-electrode units (MEU) produced and tested in this study.

MEU No	Electrodes	Separator	Sep. thickn. (µm)	Mass in the air (mg)	Wet mass (mg)	Mass gain (mg)
1	G 2mg/ml	BE 35 mg	15	39.9	42.6	2.7
2	G/BE 2ml/6mg	BE 35 mg	15	-	-	-
3	G/BE 1ml/10mg	BE 70 mg	30	87.8	92.6	4.8
4	G/BE 1ml/10mg	BE 35 mg	15	58	61.9	3.9
5	C/BE 5mg/5mg	BE 35 mg	15	-	-	-
6	G/BE/C 1ml/5mg/5mg	BE 70 mg	30	-	-	-
7	G/BE/C 1ml/10mg/5mg	BE 70 mg	30	103.3	110.2	6.9
8	G/BE/C 1ml/10mg/5mg	BE 35 mg	15	51.7	54.5	2.8
9	G/BE/C 1ml/10mg/5mg	BE 15 mg	7	34.8	38.2	3.4
10	G/BE 6ml/18mg	BE 35 mg	20	125.6	253.7	128.1
11	G/BE 10ml/18mg	BE 35 mg	20	91	619.5	528.5
12	G/BE 6ml/15mg	BE 15 mg	10	77	521.8	444.8
13	G/BE 6ml/15mg	BE 35 mg	20	77	195.5	118.5
14	C/G/BE 6ml/6ml/15mg	BE 35 mg	20	89	-	-
15	G/BE 6ml/15mg	BE 35 mg	20	77	-	-
16	G/BE 6ml/15mg	BE 35 mg	20	120	236.2	116.2
17	G/BE 6ml/15mg	BE 35 mg	20	120	289.5	169.5
18	G/BE 6ml/15mg	BE 35 mg	20	120	208	88

Note: G=graphene, BE=Bentonite (Smectite).

3. Clay's electrical properties on compactness, clay type, and water content.

The conductivity of different clays was measured under wet and dry conditions (Fig. S18). Samples exposed to saturated water vapor and those saturated with water at high pressure were compared (Fig. S19). The effect of sample compactness under high pressure was explored (Fig. S20). It was found that the conductivity of clay is generally independent of sample compactness. Large water-filled pores were found to contribute less to conductivity compared to nanopores. Additionally, the electrical conductivity of clay reaches a maximum at a relatively low water content of approximately 30% and remains stable with higher water saturation. This suggests that ionic current primarily occurs within nanometer-sized interstitial slit pores rather than within larger micro-pores. These findings are consistent with previous studies, which report maximum proton conduction and water polarizability in pores around 1 nm [1, 2]. Thus, the interlayer channels in clay provide the necessary confinement to 'activate' the electrical properties of ultraconfined water.

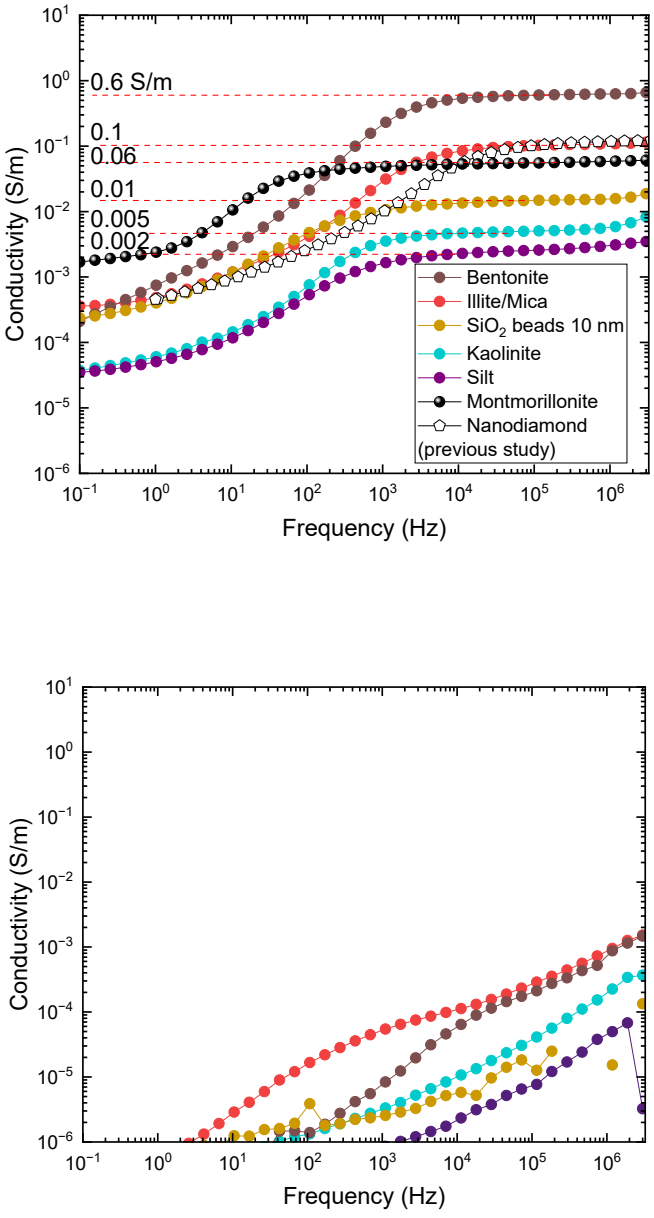

Fig. S18. Proton conductivity of clays on water content. Comparison of the proton conductivity data from Fig. 3e of the main text with that in other nanoporous materials, such as 10-nm silica beads ceramics, silt, and 5-nm nano-diamond ceramics (data from [1]). The top graph is for wet samples, the bottom graph is for the same dry samples. The dry samples were filled with water by long exposure to saturated water vapor, excluding contamination.

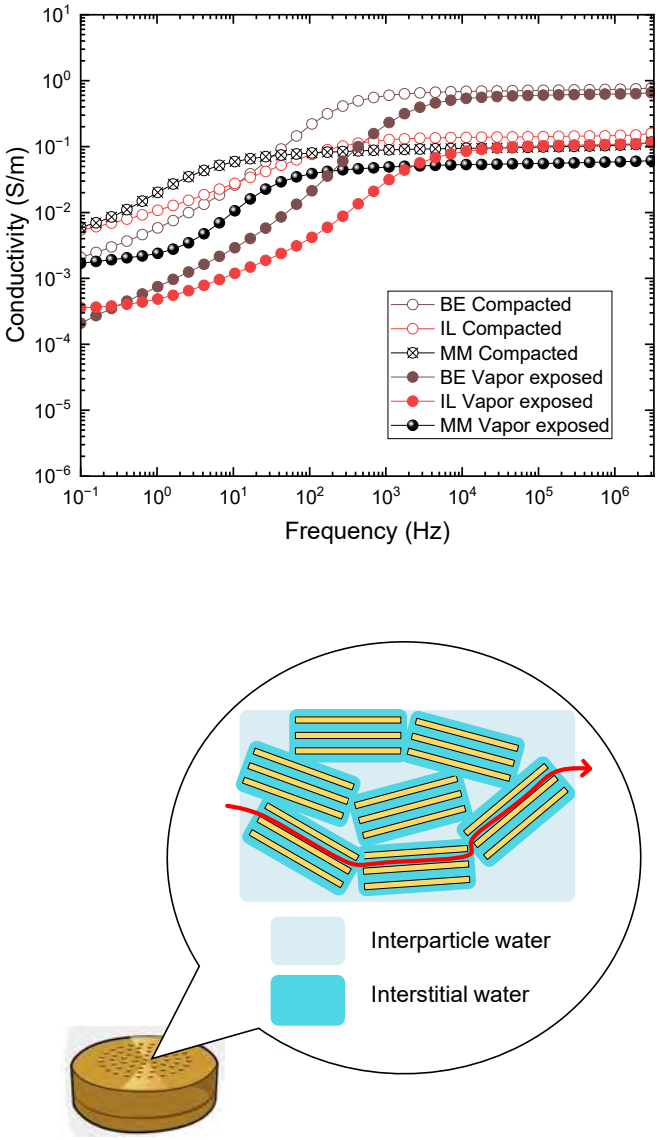

Fig. S19. Proton conductivity of clays in micro and nanopores. Comparison of electrical (proton) conductivity of the saturated-water-vapor-exposed clay samples (bentonite, illite, and montmorillonite) with that placed in liquid water under high pressure. The bottom picture shows the difference between the interstitial water between the clay crystal layers and the interparticle water in micropores between the clay particles. A minor difference between the two cases indicates that the conductivity originates from the nanopores rather than large micropores.

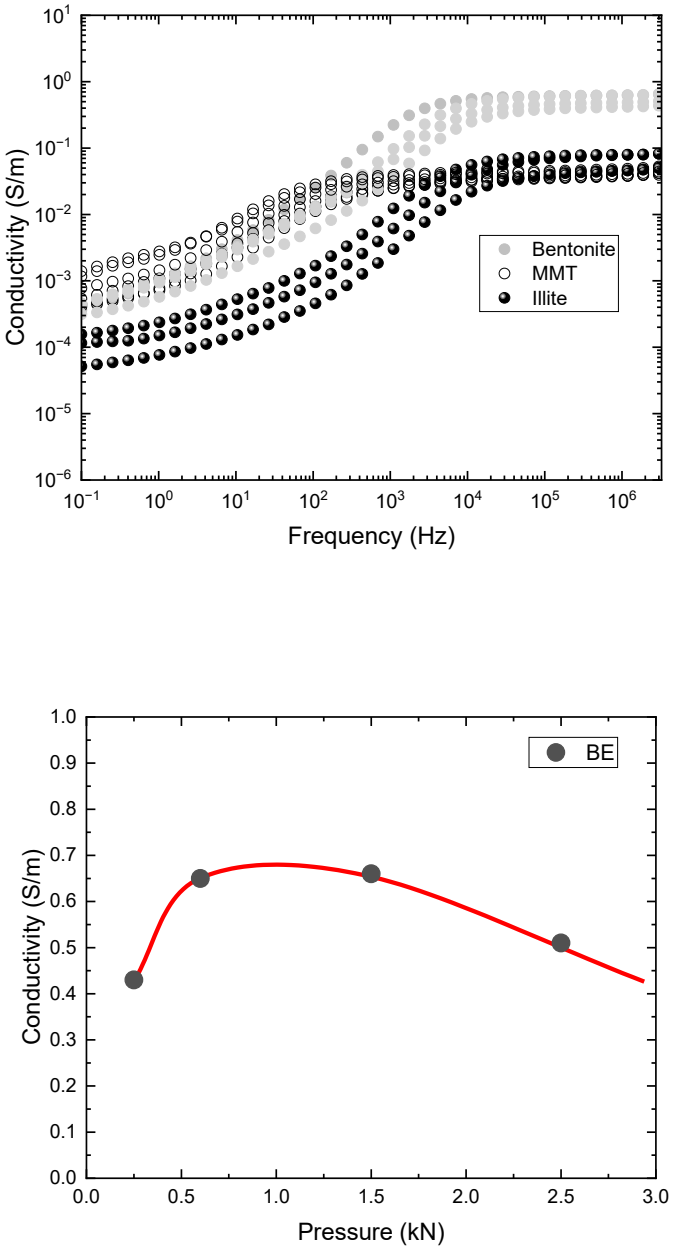

Fig. S20. Proton conductivity of clays depending on the applied pressure. The top graph shows the measurement of electrical conductivity at different pressures. The bottom graph shows the dependence of the DC conductivity plateau for bentonite clay. The red-curve fit shows that the pressure dependence of the clay proton conduction is weak. This confirms the results shown in Fig. S19 because pressure affects the large pores rather than nanopores.

4. SEM, TEM, and STEM imaging

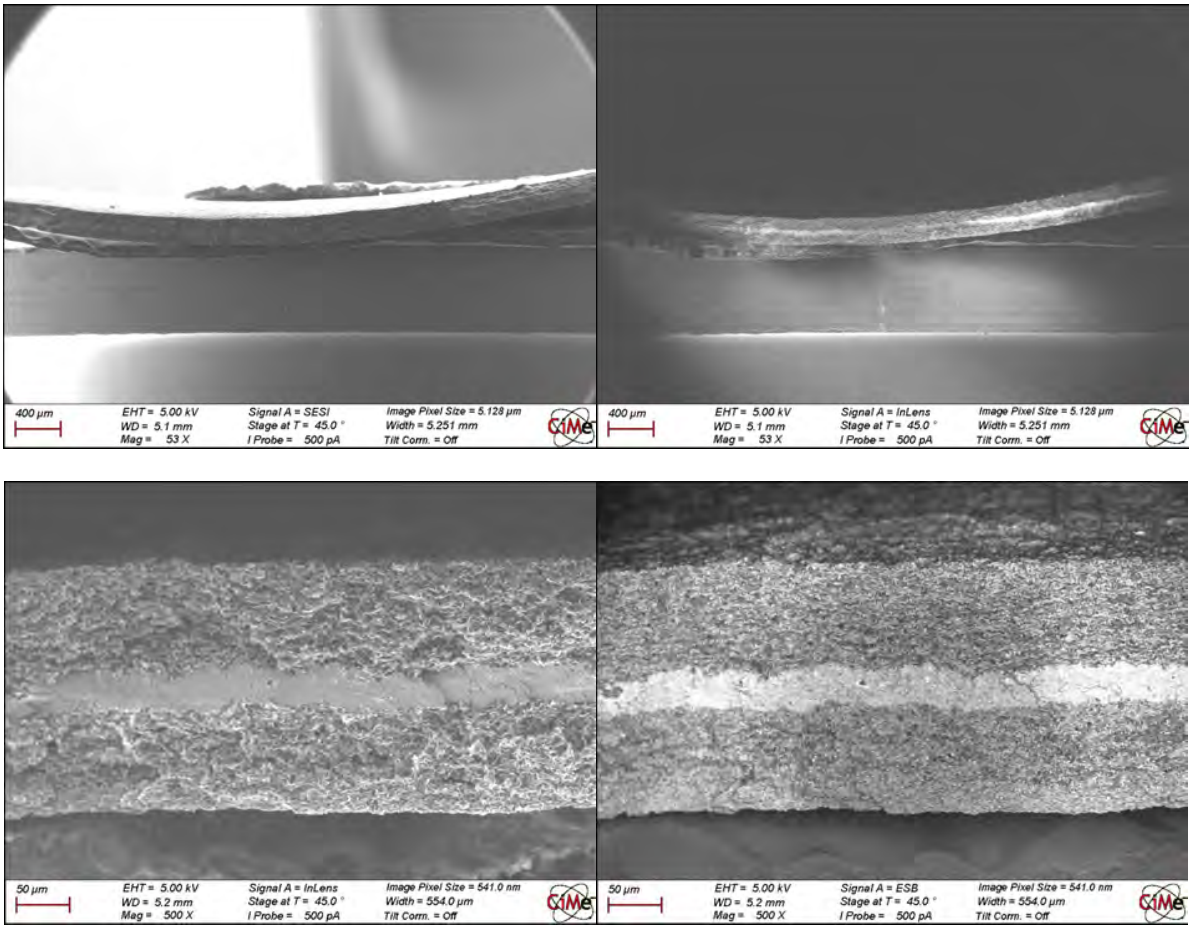

Fig. S21. SEM image of the cross-section of dry MEU10 (electrode thickness about 70 µm) at different resolutions (see scalebars and legends). Outer layers: 90% smectite, and 10% graphene. Inner layer: 100% smectite.

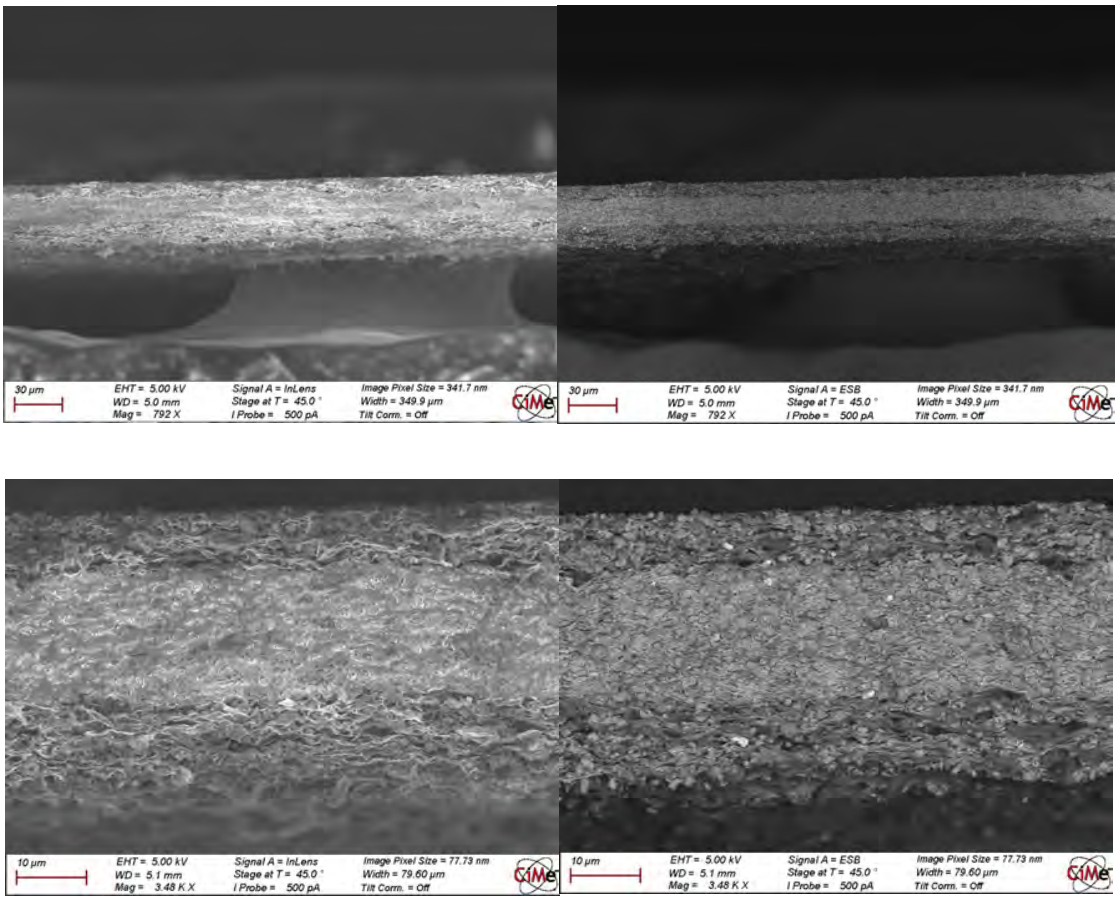

Fig. S22. SEM image of the cross-section of dry MEU4 (electrode thickness about 10 µm) at different magnifications (see scalebars and legends). Outer layers: 90% smectite, and 10% graphene. Inner layer: 100% smectite.

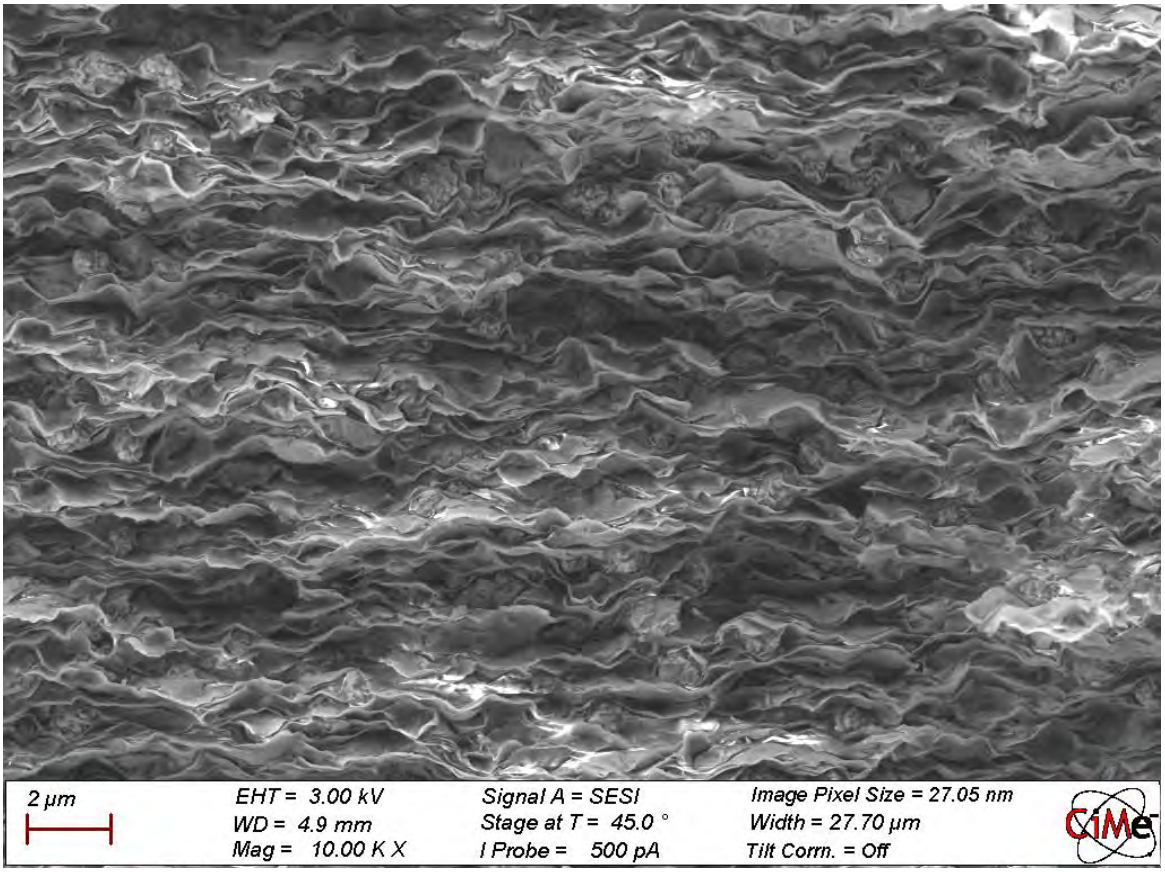

Fig. S23. SEM image of the cross-section of dry smectite membrane at different magnifications (see scalebars and legends).

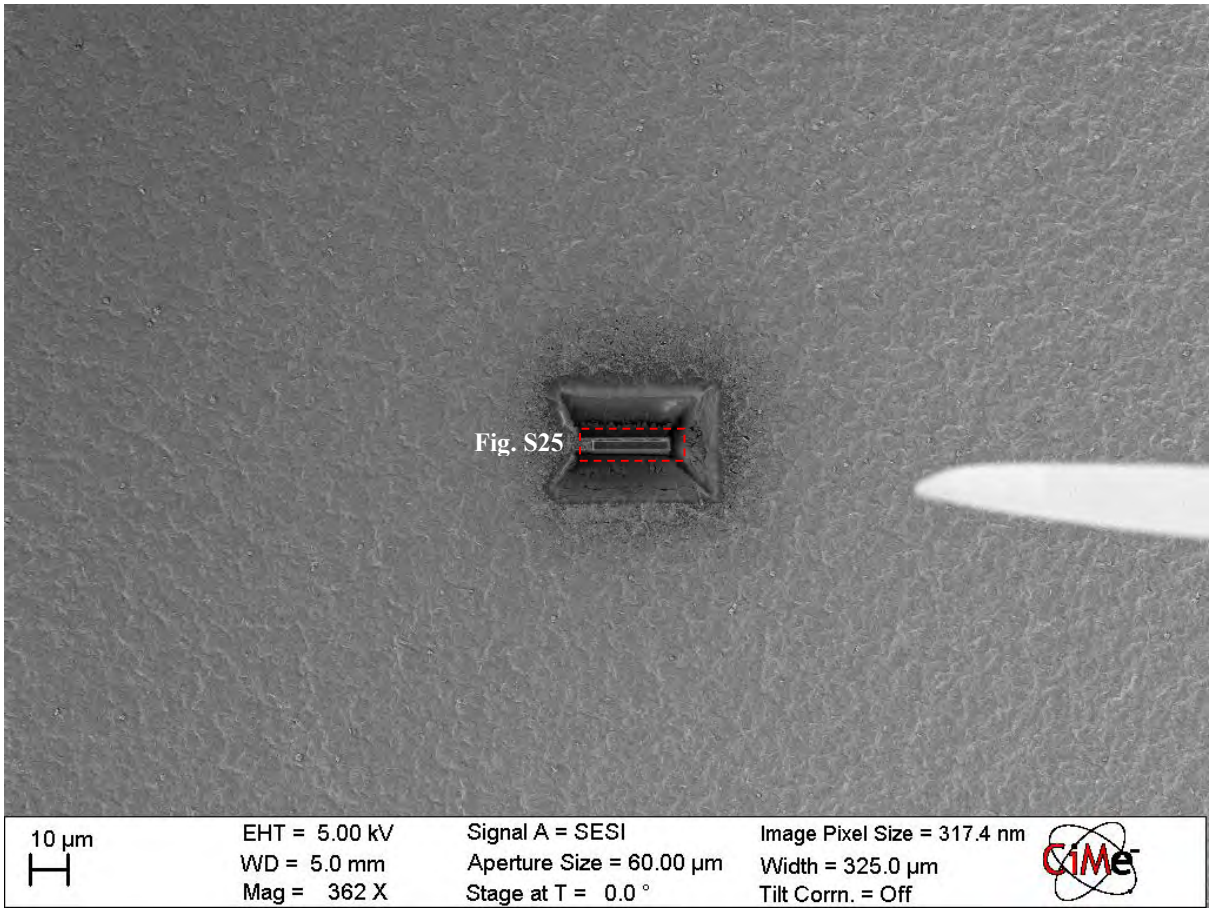

Fig. S24. SEM picture of the hole made by the Ga-focused ion beam (FIB) on the surface of a smectite membrane for TEM sample preparation. The middle part is lamella, the SEM and STEM images of which are shown in Figs. S25 and S26, respectively.

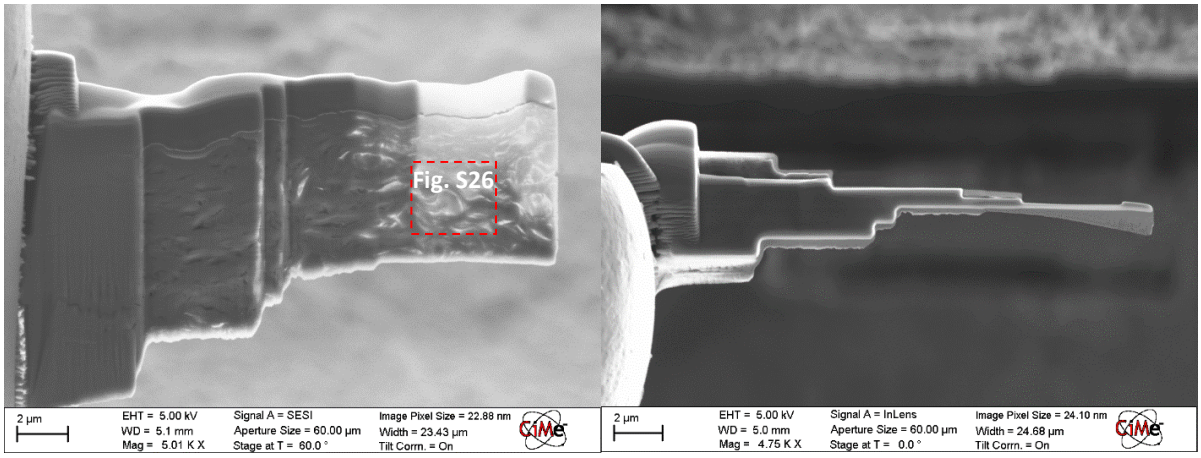

Fig. S25. SEM image of the lamella cut of smectite membrane from side (left) and top (right) views. The red square shows the part imaged by STEM in Fig. S26.

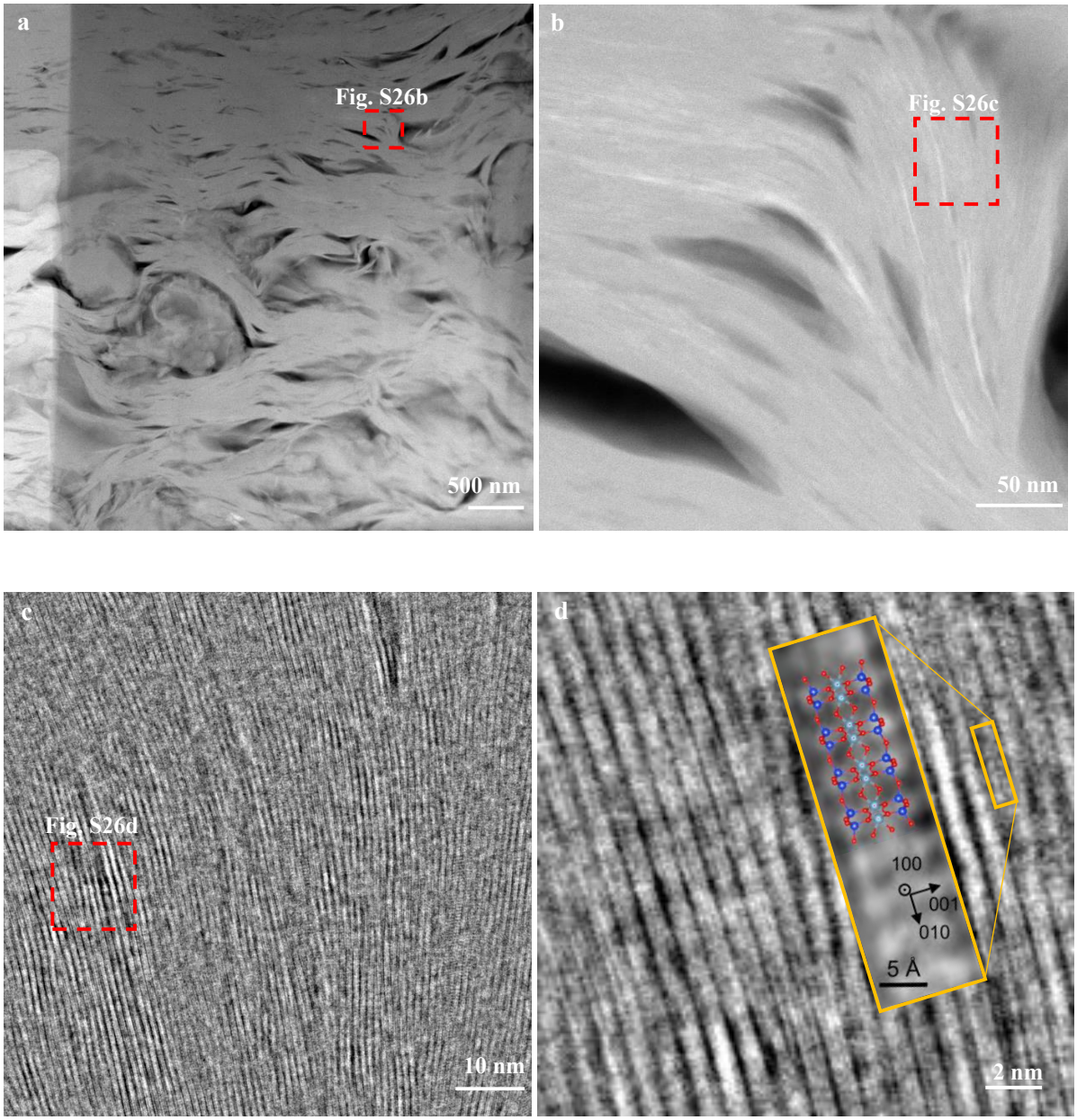

Fig. S26. STEM imaging of a cross-section of a smectite membrane at different resolutions (see scale bars). Red squares indicate the part enlarged on the next slide from left to right and top to bottom. (**a, b**) Annular dark-field (ADF) STEM images at lower magnification. (**c,d**) Integrated differential phase contrast (iDPC) STEM pictures, used to provide atomic-resolution images at the low-dose condition to prevent degradation of the crystal structure [3]. The inset shows the crystal structure overlapped on the atomic-resolution image. Red, blue, and cyan balls are for O, Si, and Al atoms, respectively.

Table S3. Comparison of the device of this study with other electricity retention technologies.

	Li-ion Batteries	Lead-Acid Batteries	Pumped Hydro Storage	Flow Batteries	Standard Supercapacitors	**This study***
Energy/Power density	High/Low	Moder./Low	Low/Moder.	Moder./Low	Moder./High	Moder./High
Lifecycle	500-3000 cycles	200-800 cycles	30+ years	~ 1000 cycles	> 5000 cycles	> 60000 cycles*
Charging time	hours	hours	days	hours	ms to minutes	μs to minutes*
Sustainability	Environmental impact, recycling challenges	Lead pollution, recycling challenges	Low environmental impact	Chemical pollution, habitat disruption	Moderate ecological impact, potential for recyclability	Natural materials, low environmental impact
Safety	Risk of thermal runaway, fire, and explosion	Risk of lead exposure, acid spills	Low risk, but potential for dam breach scenarios	Risk of chemical leakage	Low risk	Low risk
Dependence on raw materials	Rare earth elements (Li, Co, and Ni), subject to supply chain constraints and price fluctuations	Lead and sulfuric acid, subject to price fluctuations	Dependent on water resources, land availability, and regulatory approvals	Vanadium, zinc, iron, or other metal-based electrolytes, subject to supply chain constraints	Carbon-based materials, aluminum, and other metals, generally abundant and readily available	Uses readily and widely available materials, minimal risk of supply chain constraints
Applications	Portable electronics, Electric vehicles, Small-scale storage	Automobile starting and ignition batteries, Small-scale storage	Long-term energy storage from renewable sources	Backup power, short and long-term energy storage	Fluctuating loads (portable devices), Wind and photovoltaic systems peak loads shaving, Defibrillators, Transport braking energy recovery	Same as supercapacitors + Fast-frequency control, Biocompatible devices, Batteries for Mars colonization, Biodegradable batteries.

**Based on lab-scale prototype tests.*

References

[1] Artemov, V.G., Uykur, E., Kapralov, P.O., Kiselev, A., Stevenson, K.J., Ouedane, H., Dressel, M.: Anomalously high proton conduction of interfacial water. J. Phys. Chem. Lett. 11, 3623-3628 (2020)

[2] Wang, R., Souilamas, M., Esfandiar, A., Fabregas, R., Benaglia, S., Nevison- Andrews, H., Yang, Q., Normansell, J., Ares, P., Ferrari, G., Principi, A., Geim, A.K., Fumagalli, L.: In-plane dielectric constant and conductivity of confined water. arXiv preprint 2407.21538 (2024)

[3] Bosch, E.G.T., Lazic, I., Lazar, S.: Integrated Differential Phase Contrast (iDPC) STEM: a new atomic resolution STEM technique to image all elements across the periodic table. Microsc. Microanal., 22, 306-307 (2016)